Title
⟨a⟩-type Screw Dislocation Core Structure and Solute Interaction in α-Ti

Author
Rothchild, Eric Wilson

Publication Date
2022

Peer reviewed|Thesis/dissertation

$\langle a \rangle$-type Screw Dislocation Core Structure and Solute Interaction in α-Ti

by

Eric Wilson Rothchild

A dissertation submitted in partial satisfaction of the

requirements for the degree of

Doctor of Philosophy

in

Engineering - Materials Science and Engineering

in the

Graduate Division

of the

University of California, Berkeley

Committee in charge:

Professor Daryl C. Chrzan, Chair
Professor Mark Asta
Professor Peter Hosemann

Fall 2022

$\langle a \rangle$-type Screw Dislocation Core Structure and Solute Interaction in α-Ti

Abstract

$\langle a \rangle$-type Screw Dislocation Core Structure and Solute Interaction in α-Ti

by

Eric Wilson Rothchild

Doctor of Philosophy in Engineering - Materials Science and Engineering

University of California, Berkeley

Professor Daryl C. Chrzan, Chair

α-Ti and α-Ti alloys are of technological interest as high specific strength, corrosion resistant, nonmagnetic, and bio-compatible materials. However, they are costly to process and require strict control of the presence of interstitial impurities that cause significant strength gains, but also loss of ductility. This work uses atomistic simulations to examine the properties of dislocation cores, *i.e.* the regions in a material surrounding a dislocation that has been deformed beyond it's ideal strength in α-Ti and α-Ti alloys. Particular attention is paid to the interactions between these dislocations and solute atoms. It is shown that dislocation core structure affects the interaction with interstitial oxygen, and that solute atoms may be used to influence the dislocation core structure of screw dislocations through the so-called Cottrell atmosphere.

Contents

List of Figures

List of Tables

Acknowledgments

Thank you to all of my colleagues during my time at Berkeley. Much, if not all of the work in this thesis was a collaborative effort, and I will try to give the appropriate credit below:

In the updated derivation and implementation of the elastic stability parameter calculation, work was performed with contributions from Ian Winter.

The study of the interstitial shuffling mechanism was aided by Max Poschmann.

The study of Cottrell atmospheres around screw dislocations was performed collaboratively with Siying Li, with contributions from David Jany.

Many of the simulations performed here were envisioned because of results from then-members of Andrew Minor's research group - including Ruopeng Zhang, Yan Chong and Shiteng Zhao.

Lastly of course I give thanks to Mark Asta and my advisor Daryl Chrzan who oversaw the work included in this thesis.

This research was funded by the US Office of Naval Research under grant N00014-16-1-2304.

Chapter 1

Introduction

Ti and Ti alloys are an attractive class of structural materials for their high specific strength across a large temperature range, corrosion resistance, biocompatibility, and nonmagnetic properties. Because of this, they find many applications ranging from commercial and military aerospace, to medical devices and consumer goods. The use of Ti and Ti alloys is however limited by the high cost, low ductility, and low formability compared to more common structural metals such as steels and Al alloys. In α-Ti alloys, these limitations are all related to the interstitial impurity content, particularly of oxygen (Banerjee & Williams, 2013; Hurless & Froes, 2002).

Instead of strictly controlling the oxygen content to increase ductility, which is a large contributor to the cost of Ti alloys, it may be possible add substitutional solutes that limit the oxygen sensitivity. In theory, this would result in a reduced-cost, ductile Ti alloy that can still take advantage of the increased strength from oxygen interstitials.

In order to design alloys for reduced oxygen sensitivity, it is necessary to understand the mechanisms by which oxygen effects plastic behavior. The work described and proposed here will primarily focus on simulations and development of theory for the behavior of $\langle a \rangle$-type screw dislocations, their interactions with interstitial oxygen, and how that affects plastic behavior in Ti and Ti alloys. This work is a mix of atomistic simulations, both classical force-fields and Density Functional Theory (DFT), and continuum mechanics calculations.

1.1 Titanium Metallurgy

At low temperature, pure Ti takes its α phase, where it is a hexagonal close-packed (HCP) crystal. At higher temperatures there is a transition from the α to the β phase, which is body centered cubic (BCC). Certain alloying elements promote the stability of one phase over another, for example in the ubiquitous Ti-6Al-4V alloy, Al serves as an α stabilizer, and V as a β stabilizer, leading to a mixed α-β microstructure (Lütjering & Williams, 2007). I will focus on Ti in the HCP phase, and whenever Ti is written here it should be assumed to mean α-Ti unless otherwise specified. The α alloys include commercially pure (CP) Ti, as

well as Ti-3Al-2.5V, and Ti-5Al-2.5Sn alloys (Al, V, and Sn are all substitutional alloying elements).

Like many other HCP metals, Ti's primary mechanism of plastic deformation is the motion of $\langle a \rangle$-type ($\frac{1}{3}\langle 11\bar{2}0 \rangle$ in four index notation) dislocations, with $\langle c+a \rangle$-type dislocations generally inactive except at high temperatures and strains. The $\langle a \rangle$-type edge dislocations are highly mobile (Naka et al., 1988), and often progress quickly to the grain boundary, leaving long straight segments of screw dislocations in their wake. These are then the primary carriers of plastic deformation, and so the focus of our studies.

As mentioned above, α-Ti alloys often include substitutional elements at several Wt. %. Interstitial solutes on the other hand are often seen as impurities, and have profound effects on the mechanical properties even with concentrations on the order of 0.1 Wt. %. (Conrad, 1981; R. Jaffee, 1950; R. I. Jaffee et al., 1950; Vaughan et al., 1980). Oxygen in α-Ti is expected to sit in one of the octahedral (Oct) or hexahedral (Hex) interstitial sites, however density functional theory (DFT) calculations have also shown the oxygen stable in the crowdion site (Wu & Trinkle, 2011). In those calculations the Oct site had the lowest energy, followed by the Hex site (1.2 eV higher), and then the crowdion site (an additional 0.7 eV higher).

1.2 $\langle a \rangle$-type Screw Dislocations

The $\langle a \rangle$-type screw dislocations in pure Ti primarily move on the $\langle 1\bar{1}00 \rangle$ (prism) plane, and cross-slip on the $\langle 10\bar{1}1 \rangle$ (pyramidal) plane (Clouet et al., 2015). In general, the directional mobility of dislocations is controlled by the core structure of said dislocation. In the case of titanium, the high mobility of the $\langle a \rangle$-type edge dislocations may be attributed to their spreading of several Å in their slip plane (Crecy et al., 1983). The relatively low mobility of the screw dislocations is a more complicated matter, and related to polymorphism of structures of the dislocation core.

The $\langle a \rangle$-type screw dislocations in Titanium undergo irregular, or "jerky", motion due to what is called the locking-unlocking mechanism (Clouet et al., 2015). According to DFT simulations, the lowest energy configuration of the core of the $\langle a \rangle$-type dislocation is spread along the pyramidal plane, but the resistance to slip or Peierls barrier is much higher for pyramidal slip than for prismatic slip (Clouet et al., 2015; Poschmann et al., 2017, 2019). The dislocation must transform to a prismatic configuration before it can glide easily.

The behavior of the screw dislocations is even more complicated when there are interstitial impurities present. Of the two common interstitial sites for oxygen in Ti, the Oct sites are the lower energy site of the two in DFT and MD simulations (Poschmann, 2018; Wu & Trinkle, 2011). According to classical molecular dynamics (MD) simulations they are also a stronger obstacle, causing more dislocation bow-out (i.e. raising the flow stress) more than the Hex sites (Poschmann, 2018).

The profound strengthening effect of oxygen has been explained as a result of a contact interaction between the Oct oxygen and the dislocation core (Yu et al., 2015). Slip in the

prism plane destroys the octahedral interstitial site, and so oxygen has to move into the Hex site within the dislocation core.

The theoretically predicted shuffling of oxygen from the Oct to Hex interstitial site has been claimed to cause slip plane softening (Poschmann, 2018). This prediction has been corroborated by the wavy-to-planar slip transition experimentally observed with increased oxygen content, decreased temperature, or increased strain rate in close-to-pure Ti with oxygen impurities (Chong et al., 2020). Wavy-to-planar slip transitions are generally associated with slip-plane softening effects and are often a precursor to fracture because they result in a large strain localization (Koss & Chan, 1980). This is both an example of how the nano-scale structure of a material can affect macroscopic properties, and an example of how insights from theory and simulation can become an avenue for alloy design.

Through this dissertation I will discuss the various interactions between a dislocation and an interstitial atom. Suzuki segregation changes the energy of splitting into partial dislocations (Suzuki, 1962). The interaction between the screw dislocation core field an an oxygen interstitial is shown to correlate with shuffling behavior in atomistic simulations. A Cottrell atmosphere effect (Cottrell & Bilby, 1949) may change the dislocation energy based on the core spreading, stemming from an interaction with the long-ranged elastic field of partial dislocations. A diagram of these effects based on position of the solute with respect to a pair of partial dislocations is given in Fig. 1.1.

Before diving into the various phenomena that alter dislocation core energy, there is some necessary background on elasticity theory, atomistic simulations, and the visualization of dislocation core structures, which will be given in chapters 2 and 3. In the 4^{th} chapter, a relationship between dislocation core structure and dislocation-interstitial interaction is shown, and related to the elastic interaction between the dislocation core fields and the hexahedral oxygen interstitial. The interaction energy between the interstitial and the dislocation is well predicted by a simple micromechanical model, i.e. the effect is elastic in nature, at least in the empirical potential considered. In the 5^{th} chapter, a traditionally unexpected Cottrell atmosphere effect is shown around screw dislocations surrounded by octahedral oxygen, again using a simple linear elastic model.

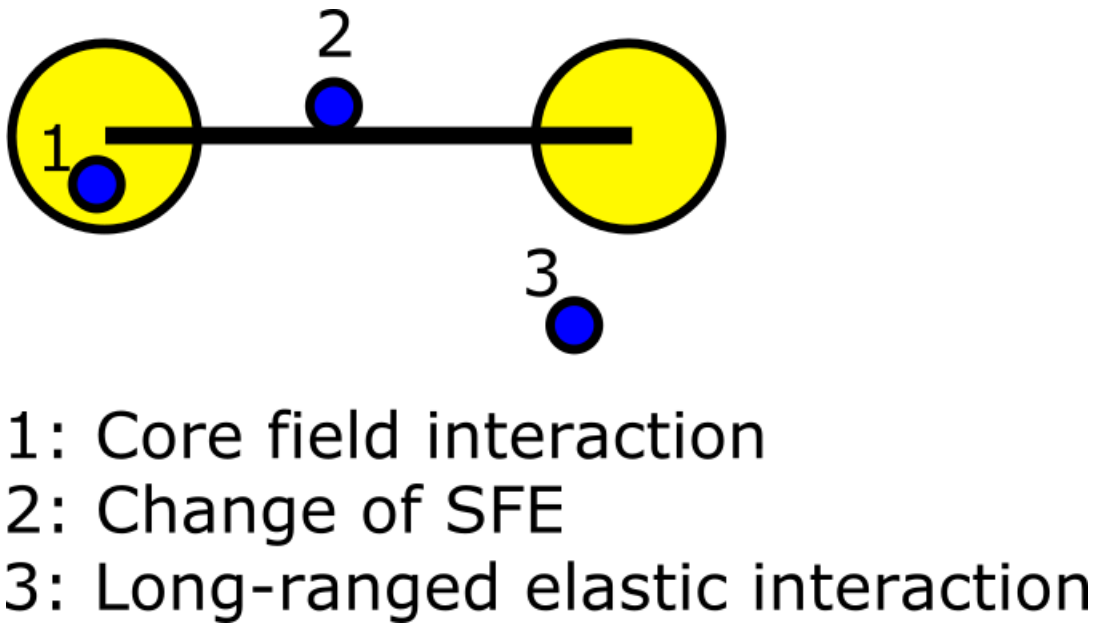

Figure 1.1: Two partial dislocations in yellow separated by a stacking fault. In blue are potential positions for interstitial atoms that would have an effect on core energy through a core field elastic interaction, a change in stacking fault energy, or a long-ranged elastic interaction.

Chapter 2

Methods

2.1 Continuum Mechanics

In contrast to the plastic deformation of materials, dominated by the motion of dislocations in the case of most metals, a materials scientist might define an elastic deformation in a material as one that is fully recoverable, without dissipation, when the applied load is removed. (Pinned dislocations could bow and unbow enabling anelastic behavior, but this would still dissipate energy). At small strains, a linear constitutive equation, Hooke's law, is used to describe the relationship between stress and strain. Using the Einstein summation convention,

$$\sigma_{ij} = C_{ijkl}\epsilon_{kl} \tag{2.1}$$

where σ is the stress, ϵ is the strain, and $\mathbf{C}$ are the elastic constants. In a later section describing the Wallace tensor, a nonlinear relationship between stress and strain will be used instead.

Around a defect such as a dislocation, Hooke's law will lead to stress diverging, unless a certain region around the dislocation is ignored. The strain field in the xy plane, of a screw dislocation in an isotropic homogeneous medium, with its Burger's vector ($\mathbf{b}$) and line direction along the z direction, can be written as:

$$\begin{aligned} \epsilon_{xz} &= \frac{-b}{4\pi}\frac{sin(\theta)}{r} \\ \epsilon_{yz} &= \frac{b}{4\pi}\frac{cos(\theta)}{r} \end{aligned} \tag{2.2}$$

where θ and r are standard directions in a cylindrical coordinate system. All other strains are zero. It is easy to see by comparing 2.1 and 2.2 that the strain (and therefore through Hooke's law both stress and energy) diverge as r approaches 0. For this reason it is common to avoid a region around the dislocation, commonly referred to as the dislocation core, when using elasticity theory in the context of dislocations or other defects.

Other times it may make sense to think of said defects as inelastic objects, separate from and imposing an inhomogeneous elastic field on an elastic body. As an easy-to-visualize example, an interstitial atom acts as a point source of dilation. This inhomogeneous field would interact with any elastic field applied homogeneously to the bulk of the medium. The study of those interactions is in the realm of micromechanics, and is important for, among other things, understanding the elastic contribution to energy in atomistic simulations (Daw, 2006). Later on, we will use some results from micromechanics to understand the interaction between interstitial atoms and dislocation cores.

2.2 Atomistic Simulations

As elasticity theory fails in the region of the dislocation core, and since the core structure has a strong impact on the mobility and dynamics of a dislocation, different methods are needed to study the core regions. The following is a brief overview of the methods used throughout this work, and the justification for their use.

Density Functional Theory

Density functional theory (DFT) is an electronic structure method that began with the works of Hohenburg and Kohn (Hohenberg & Kohn, 1964), who showed that:

1. For a of a system of interacting particles (here electrons) in an external potential, the external potential is a unique functional of the particle density.

2. By minimizing the energy with respect to variation in the particle density, one finds the electron density corresponding to the solutions of the Schrödinger equation

There has been much work in the field since then to get towards the correct, or exact, density functional. The DFT simulations performed here use the Perdew-Burke-Ernzerhof (PBE) functional form which is within the generalized gradient approximation (GGA) (i.e. uses density, and density gradient as terms) (Perdew et al., 1996). Details of calculations will be supplied as relevant.

In the field of materials science, DFT simulations have become a standard tool, as they make accurately predicting the energy of an arrangement of atoms a tractable. For understanding mechanical properties DFT is used for the calculation of elastic constants, stacking fault energies (SFE) and dislocation core structures, and a number of other properties. That said, DFT calculations scale on $\mathcal{O}(n^3)$ or $\mathcal{O}(n^2 \log n)$, where n is the number of electrons in the system, so calculations are limited to at most several hundred or thousand atoms. This is insufficient for the study of long dislocations, and important events in plastic behavior such as formation of kink pairs.

Empirical Potentials

Empirical potentials offer a less computationally expensive alternative to electronic structure methods, allowing for simulations of hundreds of thousands of atoms or more. Thus, they are an important tool in the study of defects in metals, an inherently mesoscale problem. This increase in speed comes at a cost of accuracy, and potentials may only be suitable to study a material in a certain phase or composition.

Embedded atom method (EAM) potentials are very commonly used for the study of metals and alloys. The EAM formulation assumes the energy of a system may be written as (Daw & Baskes, 1984; Daw et al., 1993):

$$E = \sum_i (F_i(\rho_i) + \frac{1}{2}\sum_{i \neq j} \phi_{ij}(r_{ij})) \tag{2.3}$$

Here F is an embedding function of the atomic electron density ρ, and ϕ_{ij} is the pair interaction between two atoms i and j at a distance r_{ij}. While classical potentials are less accurate than DFT, the computation of the energy scales linearly with the number of atoms, allowing very large systems, here tens to hundreds of thousands of atoms, to be studied.

For many of the simulations performed in this thesis, a modified embedded atom method (MEAM) type empirical potential was used (Baskes, 1992). This extends the earlier EAM formalism to include terms involving angles formed by bonds between three atoms. The MEAM simulations here were performed with the LAMMPS simulations software package (Thompson et al., 2022) and an MEAM potential specifically developed for simulating dilute oxygen interstitials in Ti (Zhang & Trinkle, 2016).

Nudged Elastic Band

The nudged elastic band method (NEB), used later in studies of the interstitial shuffling mechanism (ISM), is a method used for finding transition states that can be used with DFT or classical force fields. It works by relaxing several images of a system simultaneously, with the first and last image being local energy minimums and the images in-between being an initial guess at the minimum energy pathway between them. For example, the middle images may be linear interpolations of the positions of each atom before and after slip occurs. To find the saddle point and prevent images from all moving to the two local minimums, an extra spring force is applied to the images as they relax, so that the total force on image i is

$$F_i^T = F_i^{S\parallel} + F_i^{\perp} \tag{2.4}$$

Where $F_i^{S\parallel}$ is the spring force parallel to the local tangent between neighboring configurations, the line in configurational space connecting neighboring images, and $F_i^{\perp}$ is the component of the true force on the system of atoms perpendicular to the local tangent (Henkelman & Jónsson, 2000). In climbing image nudged elastic band (CI-NEB), after the original NEB calculation has converged, the force on the highest energy image is changed to instead drive

it up the potential energy surface which theoretically increases the accuracy of a predicted energy barrier (Henkelman et al., 2000).

2.3 Visualization of Dislocation Cores

Typical methods of describing dislocation cores are the differential displacement maps (Vítek et al., 1970) and the Nye Tensor distribution (Hartley & Mishin, 2005). The differential displacement map shows the relative displacement of columns of atoms, the magnitude of displacement proportional to the size of the arrow between the two columns. The Nye tensor comes from the negative curl of the deformation gradient (the Jacobian of motion from the undislocated to the dislocated state). The on-diagonal terms of the Nye tensor are the screw dislocation density, and the off diagonal terms are the edge dislocation density.

Other descriptors may also be used, such as the contour plot of local strain invariants or the centro-symmetry parameter (Kelchner et al., 1998). Some of these approaches have clear benefits. For example, when calculating the Nye tensor, no a-priori dislocation vector needs to be known (Hartley & Mishin, 2005) and the edge and screw components of the dislocation are easily separated. The Nye tensor has a few drawbacks as well. It relies on calculating second derivative of displacements and is very sensitive to the choice of the neighborhood used to describe the deformation around each atom, as well as an arbitrary angle fitting parameter. The differential displacement map does not suffer from this issue, but it becomes difficult and somewhat ambiguous to use when observing an extended dislocation with possible thermal noise.

Additionally, one may define the dislocation core as the heavily deformed region near the center of a dislocation, where the stress has exceeded the material's ideal strength (Chrzan et al., 2010; Sawyer et al., 2013; Winter et al., 2017). From this definition Poschmann *et. al.* studied core structure polymorphism in Ti using an elastic stability parameter (Poschmann et al., 2022). This parameter will be described in detail in the next chapter.

Chapter 3

Elastic Stability Parameter

The shape and size of the dislocation core in a material, sometimes defined as the heavily deformed region near the center of a dislocation, where the stress has exceeded the material's ideal strength (Chrzan et al., 2010; Sawyer et al., 2013; Winter et al., 2017), has significant implications for the plastic properties of said material (Takeuchi, 1999). Especially in materials where partial dislocations are not readily formed, the spread of a dislocation along a certain plane will effect how easily it slips. For example, in Ti and Zr metals, the lowest energy state of the $\langle a \rangle$-type screw dislocation cores, are extended on the pyramidal and prismatic planes respectively. This difference is thought to cause the relatively difficult and jerky glide in Ti compared to in Zr (Clouet et al., 2015).

The elastic stability parameter (Poschmann et al., 2022) describes the stability of a deformed state to further deformation relative to a reference state, as approximated using elasticity theory. Formally it is given as:

$$\upsilon = \frac{Min(Eig(C_{ijkl})) - Min(Eig(B_{ijkl}))}{Min(Eig(C_{ijkl}))} \tag{3.1}$$

where C_{ijkl} are the second order elastic constants and B_{ijkl} is the symmetric Wallace tensor. The symmetric Wallace tensor is the tensor that governs elastic stability from an already-stressed state (Morris Jr & Krenn, 2000; Wallace, 1998). Hence, if $\upsilon > 1$ there is a negative eigenvalue of the symmetric Wallace tensor, and linear elasticity theory would predict such a region to be unstable.

If the dislocation core is defined as the region where stress predicted by linear elasticity is greater than the ideal strength of the material, it can be described as the region where υ is greater than one.

Calculating υ only requires knowing the deformation gradient in the state of interest, as well as the second and third order elastic constants in the bulk. The details below describe the implementation of the parameter as a modifier in OVITO (Stukowski, 2009), a piece of software for visualization and analysis of atomistic simulations.

3.1 Detailed Equations

Elastic Equations

To derive the elastic stability parameter we begin by expressing the elastic energy change by approximation of a third order Taylor series in the Lagrangian strain (Winter et al., 2019). Terms with subscripts are to be assumed to be using summation notation.

$$\Delta E \approx \frac{1}{2!} C_{klmn}\eta_{kl}\eta_{mn} + \frac{1}{3!} C_{klmnpq}\eta_{kl}\eta_{mn}\eta_{pq} + ..., \tag{3.2}$$

The second order elastic constants C_{ijkl}, and the third order elastic constants C_{ijklmn} are the second and third derivative of elastic energy per unit reference volume evaluated at zero Lagrangian strain η_{kl}.

$$C_{klmn} = \frac{1}{V_0}\left(\frac{\partial^2 E}{\partial\eta_{kl}\partial\eta_{mn}}\right)_{\eta=0} \tag{3.3}$$

$$C_{klmnpq} = \frac{1}{V_0}\left(\frac{\partial^3 E}{\partial\eta_{kl}\partial\eta_{mn}\partial\eta_{pq}}\right)_{\eta=0} \tag{3.4}$$

Symmetric Wallace Tensor

The symmetric Wallace tensor is given by (Morris Jr & Krenn, 2000; Wallace, 1998)

$$B_{ijkl} = C_{ijkl} + \frac{1}{2}(\tau_{ik}\delta_{jl} + \tau_{il}\delta_{jk} + \tau_{jk}\delta_{il} + \tau_{jl}\delta_{ik} - \tau_{ij}\delta_{kl} - \tau_{kl}\delta_{ij}) \tag{3.5}$$

Where δ_{ij} is the Kronecker-delta function and τ_{km} is the Second Piola-Kirchoff stress tensor. If starting from an initially unstressed state it is easy to write τ in terms of strain.

$$\tau_{ij} = C_{ijkl}\eta_{kl} + \frac{1}{2} C_{ijklmn}\eta_{kl}\eta_{mn} \tag{3.6}$$

When at finite strain, C_{ijkl} is replaced by the elastic constants at finite deformation (ECFD).

$$C'_{ijkl} = \frac{1}{V(\eta)}\left(\frac{\partial^2 E}{\partial\beta_{ij}\partial\beta_{kl}}\right) \tag{3.7}$$

$V(\eta)$ is the volume at a strain equal to η. β is an infinitesimal strain.

Definition of Deformation Terms

To clarify the above equations, and to be able to make the elastic stability parameter a function of deformation gradient only, we need to define three states. The first state corresponds to non-deformed bulk material, with positions given as $\mathbf{X}$. The second state is finitely deformed and has positions given by $\mathbf{x}$. The third state is the result of some infinitesimal

deformation of the second and has positions given by $\bar{\mathbf{x}}$. The deformation from the first state to the second is given by:

$$F_{km} = \frac{\partial x_k}{\partial X_m} \tag{3.8}$$

$\mathbf{F}$ is a deformation gradient. The Lagrangian strain is then $\eta = \frac{1}{2}(\mathbf{F}^t\mathbf{F} - \mathbf{I})$.

The deformation gradient from the second to the third state is:

$$f_{km} = \frac{\partial \bar{x}_k}{\partial x_m} \tag{3.9}$$

And in the limit of infinitesimal strain and infinitesimal rotation:

$$f_{kl} = \delta_{kl} + \beta_{kl} \tag{3.10}$$

Where β_{kl} is an infinitesimal strain as previously mentioned.

Similarly, from the first to the third state, the deformation gradient is written:

$$\bar{F}_{km} = \frac{\partial \bar{x}_k}{\partial X_m} = f_{kl}F_{lm} \tag{3.11}$$

Combining equations (3.2) and (3.7), we can express the ECFD as:

$$C'_{ijkl} = \frac{1}{J(\eta)}\left[(C_{mnpq} + C_{mnpqrs}\eta_{rs})\left(\frac{\partial \bar{\eta}_{mn}}{\partial \beta_{kl}}\frac{\partial \bar{\eta}_{pq}}{\partial \beta_{ij}}\right)_{\bar{\eta}=\eta} + \left(C_{mnpq} + \frac{1}{2}C_{mnpqrs}\eta_{rs}\right)\left(\frac{\partial^2 \bar{\eta}_{mn}}{\partial \beta_{ij}\partial \beta_{kl}}\right)_{\bar{\eta}=\eta}\eta_{pq}\right], \tag{3.12}$$

Here $J(\eta) = Det(\mathbf{F})$ is the Jacobian of motion. Through some manipulation we can express the two derivative terms as functions of the deformation gradient.

$$\left(\frac{\partial \bar{\eta}_{ij}}{\partial \beta_{pq}}\right)_{\bar{\eta}=\eta} = F_{ki}F_{mj}I_{kmpq}. \tag{3.13}$$

$$\frac{\partial^2 \bar{\eta}_{ij}}{\partial \beta_{pq}\partial \beta_{rs}} = \frac{1}{2}F_{ki}F_{mj}\left(I_{knrs}I_{nmpq} + I_{nmrs}I_{knpq}\right), \tag{3.14}$$

Now the ECFD, and therefore the symmetric Wallace tensor at finite strain, can be calculated with only the deformation gradient and the second and third order elastic constants.

Definition of Deformation gradient on a Small Scale

From the above section it can be seen that only calculation of the deformation gradient, and use of previously known constants, is necessary to calculate υ. At the atomic scale, it is hard to define a single correct way to calculate this deformation gradient. In the implementation of the elastic stability calculation in OVITO, we use the least-squared method as in the “Atomic Strain" modifier (Falk & Langer, 1998a; Shimizu et al., 2007), but with some alterations.

In a least-squares approach the deformation gradient is given below. The equation here is not using summation notation, rather the subscript i refers to the i'th atom, and j to the j'th atom within some cutoff distance from the i'th atom.

$$\mathbf{F}_i^t = (\sum_j \mathbf{d}_{ji}^{0t}\mathbf{d}_{ji}^0)^{-1}(\sum_j \mathbf{d}_{ji}^{0t}(\mathbf{d}_{ji} - \mathbf{m}_{ij})) \tag{3.15}$$

Ignoring the terms $\mathbf{m}_{ij}$, which do not normally appear in the least-squares equation for atomic strain, the above equation gives a best fit mapping of directed distances $\mathbf{d}_{ij}^0$ between atom i and its j neighbors in a reference frame, to the directed distances $\mathbf{d}_{ij}$. With burgers vector $\mathbf{b}$:

$$\mathbf{m}_{ij} = round(\frac{\mathbf{d}_{ij} - \mathbf{d}_{ij}^0}{|\mathbf{b}|})\mathbf{b}. \tag{3.16}$$

Including the $\mathbf{m}_{ij}$ terms acts to remove shifts of a full lattice vector from the calculation of the deformation gradient.

3.2 Implementation in OVITO

General Information

The above method to calculate ν was implemented as a modifier in OVITO. This edited version of OVITO makes use of an additional dependency: the Eigen Tensor Libraries. Python bindings were created with PyBind11 for use with the OVITO Python interpreter OVITOS.

The modifier requires two supercells as inputs. The first is the strained state of interest, the second is a reference state which should match the active frame before before plastic or elastic deformation has occured.

Usage in Graphical Mode

To use the elastic stability modifier in graphical mode, first select "Atomic Strain Mod Burgers" from the "Add Modification" menu. In the panel for this modification, select an appropriate reference file, select the option to output deformation gradients, set a cutoff radius, and input the burgers vector in Cartesian coordinates. Then from the "Add Modification" menu, select the "Elastic Stability" modifier. Select the symmetry of the cell from the drop-down menu, currently only HCP and cubic crystals are supported. Once the symmetry is selected there should be input boxes for various elastic constants.

The code assumes the elastic constants are from a "typical" symmetrized reference frame. See, for example, Appendix A in Clayton's *Nonlinear Mechanics of Crystals* (Clayton, 2011) for the detailed description of the "typical" form of these tensors.

Lastly, in the box that says "Enter transformation from typical to current directions" the user must input the transformation matrix that goes from the "typical" frame to the current

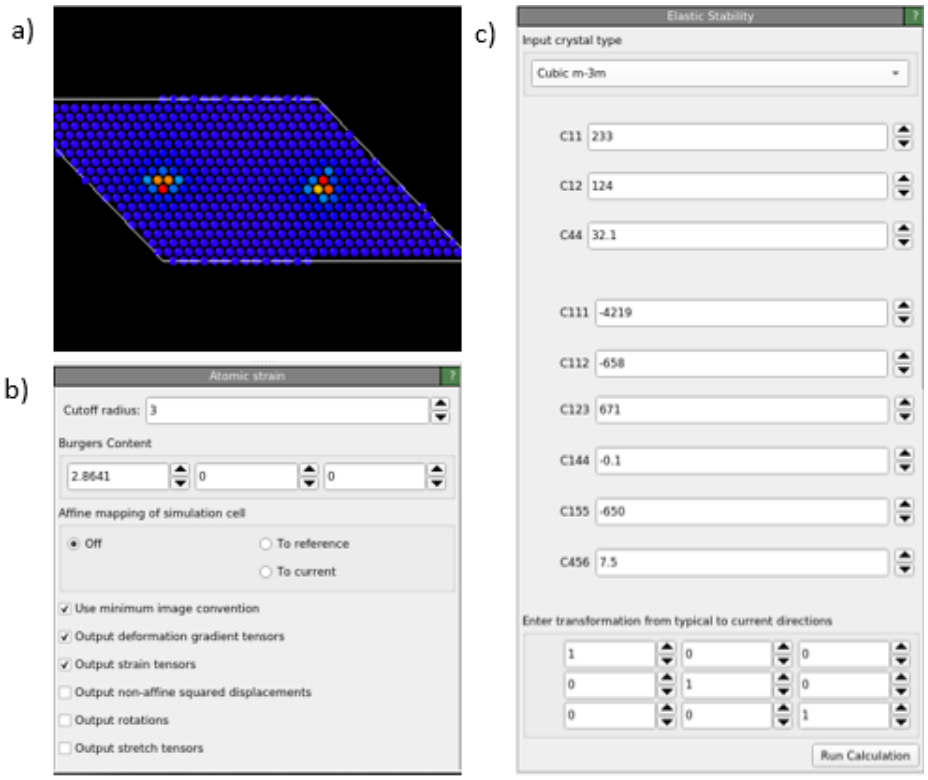

Figure 3.1: Various screenshots from the OVITO program using the “Elastic Stability" modifier. a) Atoms color coded by elastic stability to show a screw dislocation dipole in Niobium. b) Menu details of the “Atomic Strain Mod Burgers" modifier. c) Menu details of the “Elastic Stability" modifier.

coordinates. After all this is entered, pressing the “run calculation" button on the modifier panel will calculate the Elastic Stability modifier on a per-atom basis.

Python Interface

This modifier can be accessed with the OVITOS Python interpreter in the same fashion as other modifiers.

The class for the “Atomic Strain Mod Burgers" modifier is *ovito.modifiers.AtomicStrainModBurgers*. The properties for this modifier are *burgersContent*, *output_deformation_gradients*, and *output_strain_tensors*. *burgersContent* should be set to a length 3 list with floats matching the Burgers vector in Cartesian coordinates. The other properties should be set to *True*.

The class for the Elastic Stability Modifier is *ovito.modifiers.CalculateElasticStability*. Its property *set_structure* should be set to *CalculateElasticStabilityModifier.Lattice.Hexagonal_High* for HCP crystals, or *CalculateElasticStabilityModifier.Lattice.Cubic_High* for FCC or BCC

crystals. The properties *set_soec* and *set_toec* should be set as lists of the second and third order elastic constants repspectively. The input order for elastic constants matches that in the graphical interface. The final property *set_transformation_matrix* should be set to the 3x4 transformation matrix (3x3 rotation, with a translation that is ignored) that transforms from the coordinates of the “typical" frame to the current coordinates.

3.3 Discussion

The elastic stability parameter and the code implemented here are another tool for the classification of dislocation cores. This has planned uses in further analysis of the Cottrell atmospheres in Chapter 5. Equations 3.15 and 3.16 will be used in Ch. 4 to calculate strain fields around dislocation cores to understand interstitial attraction to core fields.

Chapter 4

Core Structure and Interstitial Shuffling

Planar slip is generally caused by a slip-plane softening effect in an alloy, often from short-ranged ordering (Gerold & Karnthaler, 1989; Wolf et al., 1994). Planar slip bands are considered to be a cause or precursor of fracture (Koss & Chan, 1980). This effect has been observed in experiments of Ti-alloys (Williams & Luetjering, 1980). The work in this section examines the claim that oxygen causes slip plane softening, embrittling Ti, through an interstitial shuffling mechanism (Chong et al., 2020). This section is an adaptation of previously published work (Rothchild et al., 2022).

4.1 Background

The bypassing of an oxygen-interstitial by $\langle a \rangle$-type screw dislocations in Ti is studied as a function of the dislocation core structure using an empirical potential and the nudged elastic band method (NEB). Dislocation core structure in the MEAM potential used (Zhang & Trinkle, 2016) may be controlled by the applied non-Schmid stress. It is shown that an interstitial oxygen will be pushed from the octahedral site into a new interstitial site in the dislocation core. From there, the barrier to return the interstitial oxygen to the octahedral site is of interest. If there is a high barrier to return, then interstitial shuffling is likely. Where there is little to no barrier for return, the shuffling is less likely.

To study these shuffling events, NEB simulations are performed for the case of no non-Schmid stress, *i.e.* with a prism-dissociated core, and under 3 GPa of non-Schmid stress, where the pyramidal core is most stable (at zero temperature). The simulations suggest that interstitial shuffling is likely when the prismatic core is favored, and unlikely when the pyramidal core is favored. For the purposes of this study, NEB calculations are preferable to molecular dynamics (MD) simulations as the high strain rates necessarily used in MD can lead to behaviors that are not relevant at lower strain rates. However, the results of MD simulations presented in the appendix are consistent with the predictions of NEB

calculations.

Additionally, the interaction energy between the interstitial sites and strain fields around the dislocation core are calculated with a micromechanical model. This model shows an attractive elastic interaction between the dislocation and interstitial oxygen along the prismatic direction. The attractive interaction between the hexahedral oxygen and the dislocation core is stronger for the prismatically spread core than the pyramidally spread one, which is an explanation of the increased propensity for shuffling in the prismatic case.

4.2 Methods

NEB Simulations

Dislocation dipoles were placed into supercells using Daw's solution for a periodic array of dislocations (Daw, 2006), with a deformation applied to the whole supercell to account for the distortion of the dislocations as prescribed by Lehto and Öberg (Lehto & Öberg, 1998). With one dislocation in a constant position, the other was placed at sites ranging from two c to the left to two c to the right of the interstitial atom, where c is the height of the unit cell. (There is a local minimum in the energy for motion by $c/2$ stemming from the symmetry of the hexagonal-close-packed structure.) These cells were dislocation quadrupoles with two dislocations per cell, described as an O arrangement (Clouet, 2012). Each cell was 32 [0001] by 16 $\left[1\bar{1}01\right]$, and either $3b$, $15b$, $30b$, or $60b$ deep, the Burger's vector b being $\frac{1}{3}\langle 11\bar{2}0\rangle$. For simulations including oxygen atoms, there was an octahedral or hexahedral interstitial oxygen placed in the prismatic glide plane adjacent to one of the two dislocations in the cell (as shown in Fig. 4.1).

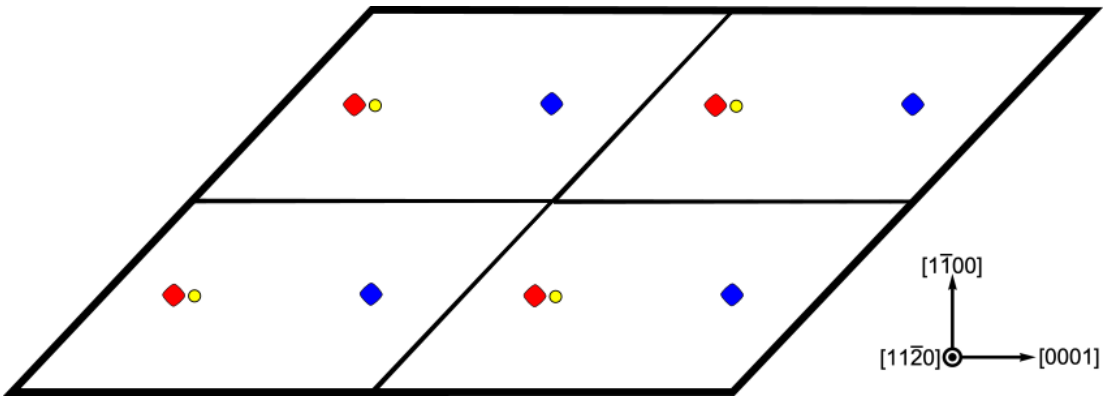

Figure 4.1: A diagram of quadrupole arranged dislocations used for the NEB simulations. Red and blue diamonds mark dislocations of opposite sign before prismatic displacement. A yellow marks the position of the oxygen. When the left dislocation has slipped on top of the oxygen, by moving 2 c, the arrangement is perfectly quadrupolar.

All energy calculations and NEB simulations were performed using LAMMPS (Henkelman & Jónsson, 2000; Henkelman et al., 2000; Maras et al., 2016; Nakano, 2008; Thompson et al., 2022). First, the cells were relaxed using conjugate gradient minimization. Due to the variety of possible core structures, exact placement of the dislocation core affected the energy of the initial relaxation, so many trials with slightly varied initial positions were considered. Linear interpolations of the lowest energy results of the above relaxation were used as starting points for the NEB calculations.

NEB simulations were performed in two stages. The first stage included nine images, starting from the linear interpolation of the initial relaxations. Several cases were considered: no oxygen, oxygen in the Hex site throughout, oxygen starting in the Oct site and ending in the Hex site, and oxygen starting and ending in the Oct site. In the simulations for cells $3b$ deep with the oxygen atom starting and ending in the Oct site, it was found that the oxygen slipped into the Hex site halfway through the 8 slip events, before returning to the original site. In order to get calculations to converge for Oct→Oct case in cells deeper than $3b$, it was necessary to have an initial pathway with the oxygen atom in the Hex site halfway through the path.

The second stage used, as a starting configuration for the NEB calculation, 41 images linearly interpolated between the nine image pathway determined in the first stage. All NEB calculations were converged to a minimum force of $1.6 * 10^{-6}$ eV/Å per atom using fire minimization. For this process the NEB force with a spring constant of 1 eV/Å was only applied to atoms within a 15 Å circular region around the dislocation at the midpoint of the slip events. It has been suggested that limiting the number of atoms the NEB force is applied to may lead to more accurate results for Peierls barriers and stresses (Gröger & Vitek, 2012).

As will be shown later, the results of the calculation above have a sharp or discontinuous energy pathway when the octahedral atom moves to or from the core interstitial site. In order to more clearly examine the behavior during the transition back to the octahedral site, a set of calculations using climbing image NEB (CI-NEB) were performed. These used final images from the original 41 image NEB simulation, starting from the Oct→Hex path (i.e. where interstitial shuffling has occured) and ending on the Oct→Oct path (where interstitial shuffling has not occured). These are calculated to be compared with the Oct→ Hex path described before. If there is a high barrier to return to the octahedral site a dislocation would be expected to leave hexahedral interstitials in it's wake. For most of these calculations, 8 images from a linear interpolation of the start and end structures were used. The NEB force was applied to the same atoms as in the first set of NEB calculations, however the spring constant was increased to 5 eV/Å, and a parallel spring constant of 1 eV/Å was also applied. For the second return paths under no non-Schmid stress 41 images were used, the first and last of which had a spring constant of 100 eV/Å applied as the first image was not a metastable position and more images were required for convergance of the simulation. Additionally the spring constant on the middle images was reduced to 1 eV/Å.

The position of the dislocation at each point in the NEB was calculated, first by evaluating the Nye tensor (Hartley & Mishin, 2005) at each atom using the Babel software package

(Clouet et al., 2009). Then, the values of the screw component were averaged along the dislocation line direction, and the center of Burgers vector density was computed (accounting for the periodic boundary conditions (Bai & Breen, 2008)). This center was what is referred to as the dislocation position for each of the NEB-determined minimum energy paths.

For comparison of energies between the far field and near-dislocation interstitial atoms, calculations were performed using similar cells to the $15b$ case, but with no dislocation present. The cases considered were, once again, the presence of an octahedral insterstitial, a hexahedral interstitial, or no oxygen atom.

Micromechanics

A micromechanical approach can be used to better understand the origin of the interaction between the interstitial atoms and the dislocations. Within this approach, the elastic interaction energy between an interstitial atom and a strain field may be computed according to (Siems, 1968):

$$E_{int} = -P_{ij}\epsilon_{ij}(x) \tag{4.1}$$

Where P is the elastic dipole tensor of the interstitial atom at position x, and $\epsilon(x)$ is the strain at position x produced by the dislocation.

The elastic dipole tensors for hexahedral and octahedral oxygen in the MEAM potential were calculated using the Kanzaki method by Poschmann (Hayward et al., 2012; Poschmann, 2018). The resulting elastic dipole tensors are (in eV):

$$P_{oct} = \begin{bmatrix} 2.71 & 0 & 0 \\ 0 & 2.71 & 0 \\ 0 & 0 & 5.72 \end{bmatrix} \tag{4.2}$$

$$P_{hex} = \begin{bmatrix} 12.48 & 0 & 0 \\ 0 & 12.48 & 0 \\ 0 & 0 & 4.19 \end{bmatrix}. \tag{4.3}$$

As there is no off-diagonal component for either the octahedral or hexahedral oxygen, there is no elastic interaction between these defects and an ideal Volterra screw dislocation. However, as shown in Fig. 4.2, there is significant spreading of these dislocation cores, and thus there may be tensile components of the core fields that would interact with the interstitial atoms. To account for these core fields, the strain fields used in the micromechanics calculation is taken from the atomic positions of dislocated cells after their potential energy is minimized.

For the calculation of the strain field around the dislocation, dislocated cells with the same arrangement as those for the NEB calculations were used were used. For these calculations there was no oxygen present and the length and height of the cell were doubled. The extra width and height was used so that the long range nature of the interaction between the dislocations and the interstitial atoms could be visualized without significant overlap of the dislocation strain fields. The cells used were 1 **b** deep. The strain in the dislocated cells after

relaxation was calculated a version of the atomic strain modifier in OVITO (Falk & Langer, 1998b; J. Li & Shimizu, 2005; Stukowski, 2010), edited as in Eqns. 3.15 and 3.16. Because the strain calculated this way is based on atomic positions from simulation, it contains non-shear terms that may interact elastically with a point-source of dilation.

4.3 Results

NEB of eight slip events

The NEB simulations of eight slip events of distance c/2 along the prism plane, which begin two c from the interstitial site and end two c away on the other side, show several interesting features. As seen in Fig. 4.3, the hexahedral oxygen has an attractive interaction with the dislocation that extends over a medium-long range - at least 10 Å. This attraction is stronger for the prismatic core than for the pyramidal core.

The octahedral oxygen primarily has a repulsive interaction with the dislocation for both the prismatic and the pyramidal spread dislocation, qualitatively matching DFT predictions (Chaari et al., 2019). However, there is a site adjacent to the dislocation core where there is an attraction between the interstitial and the dislocation which is shown in Fig. 4.4. This attractive site exists for both core structures and comes with significant rearrangement of the core structure at high oxygen density along the line. Where the interaction is stronger, under non-Schmid stress, there is basal spreading of the dislocation in the 3b deep case, and pyramidal in the longer cells. In the unstressed case a more complicated core structure is seen instead (see Fig. 4.4A). However, further studies are necessary to understand the origin of this interaction. One should note that there is a severe underestimate of the basal stacking fault energy in this MEAM potential (170 mJ/m^2 compared to 300 mJ/m^2 in DFT) (Hennig et al., 2008), and it is unclear from these results whether this effect is likely outside of MEAM simulations.

These attractions change the relative energies of the hexahedral and octahedral interstitial atoms as the dislocation approaches. This is shown in Table 4.1, where the far field values refer to the energy of the interstitial in a non-dislocated cell, the adjacent Oct site is the octahedral site directly adjacent to the dislocation core in the slip plane and the core site is when the oxygen sits in the site within the dislocation core (the adjacent Oct site is shown in 4.4, and the Hex core site in 4.6). Note that the values in the table are measured relative to the energy of an oxygen atom at the Oct site in a dislocation-free crystal. In the case of the prismatic core, the chosen cell is stress-free. In the case of the pyramidal dislocation core, the reference cell has the 3 GPa non-Schmid stress applied. From the far field calculation, the application of the non-Schmid stress increases the relative energy of the oxygen at the Hex site by 60 meV. In comparison, the energy of an oxygen atom at the core site increases by 380 meV in the pyramidal core vs the prism.

In both cases, when the dislocation pushes the oxygen into the core interstitial site, it becomes prismatically spread, as shown in Fig. 4.6A. The prismatic spread is more pronounced

Core	Far Field Oct	Far Field Hex	Adjacent Oct	Core Site
Prism	0	1.20	-0.2	0.16
Pyr	0	1.26	-0.15	0.54

Table 4.1: Relative energies in eV of the various interstitial sites for conditions under which differing cores are stable. The calculations in the prismatic core have no stress applied to the cell. For the pyramidal core, a compressive stress of 3 GPa is applied along the $[1\bar{1}00]$ direction. Values in each row are measured relative to the energy of the far field octahedral interstitial site.

in the absence of non-Schmid stress shown in Fig. 4.6D.

Examination of the the prismatic core shows that the dislocation remains unkinked, even in the $60b$ deep cells, the largest considered here. In contrast, the pyramidal cores only remained straight in the $3b$ and $15b$ cases, whereas the deeper cells displayed the formation of kinks.

NEB of return paths

The NEB paths identified above for the case of shuffling from the octahedral to hexahedral site necessarily show a net increase in energy because the energy of the interstitial atom itself is increased. Although the hexahedral autocite is higher energy, the barrier to return to the octahedral autocite away from the dislocation is non-negligible (0.85 eV according to DFT calculations (Wu & Trinkle, 2011)), and so at an appropriate strain rate, if oxygen is shuffled by the dislocation it may remain in that autocite long enough for the next dislocation to encounter it.

However, the barrier to return to the lower energy octahedral site within the dislocation core may be lower depending on dislocation core structure. To assess this barrier, CI-NEB simulations were performed starting from positions along the NEB pathway where the oxygen atoms starts in the octahedral site and ends in the hexahedral site, and ending at two positions along the NEB pathway where the oxygen starts and ends in the octahedral site. These simulations were performed using cells $15b$ deep, as that was the deepest simulation cell without significant bowing or kink formation in the pyramidal dislocations in the absence of oxygen and therefore represents how a straight segment of a dislocation would interact with the interstitial obstacle.

In addition, these calculations were repeated with cells under shear (Schmid) stress. Peierls stresses (τ_p) were roughly estimated from the original NEB calculations without oxygen by using the greatest increase in in energy during the slip event when the dislocations were closest to a perfect quadrupolar arrangement and the formula:

$$\tau_p = \frac{\Delta E}{\Delta u b^2} \tag{4.4}$$

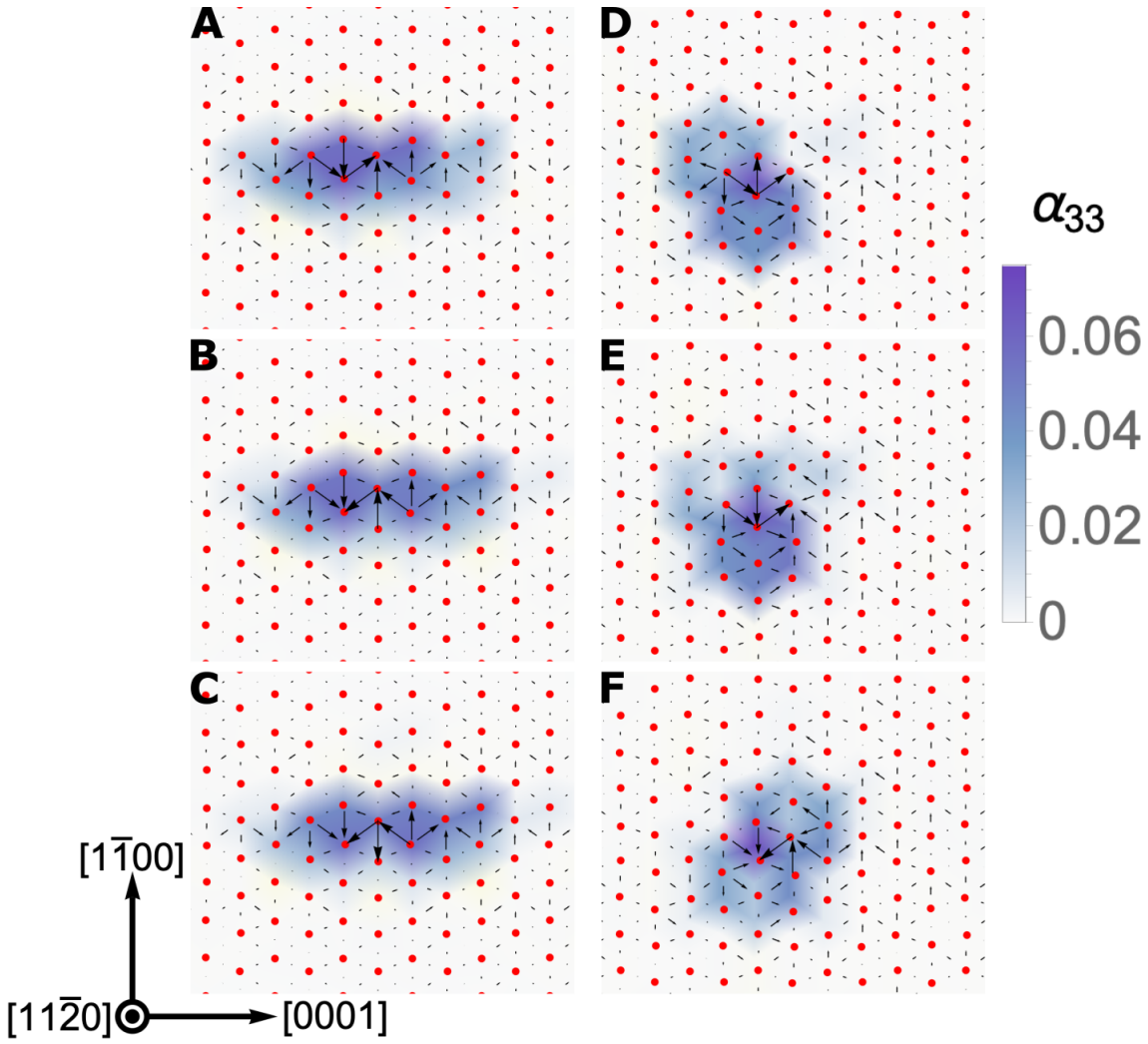

Figure 4.2: The screw component of the Nye tensor, as well as the differential displacement map are displayed to show the dislocation spreading in the absence of oxygen. A-C show the non-stressed prismatic core as it goes from the low energy state (A) to the high energy state (B) to the low energy state on the other side. D-F show the Schmid-stressed pyramidal core as it goes from low energy state (E) to high energy contracted state (E) to the low energy state (F). Note that the slip distance in going from A-C and D-F is $c/2$.

where ΔE, Δu, and b are the change in energy, change in position, and magnitude of Burger's vector respectively. The Peierls barrier for the prismatic core was estimated as 40 MPa, and for the pyramidal core as around 200 MPa. NEB simulations for the return paths were performed repeated at half of the estimated Peierls barrier, 20 and 100 MPa respectively for the prismatic and pyramidal cores.

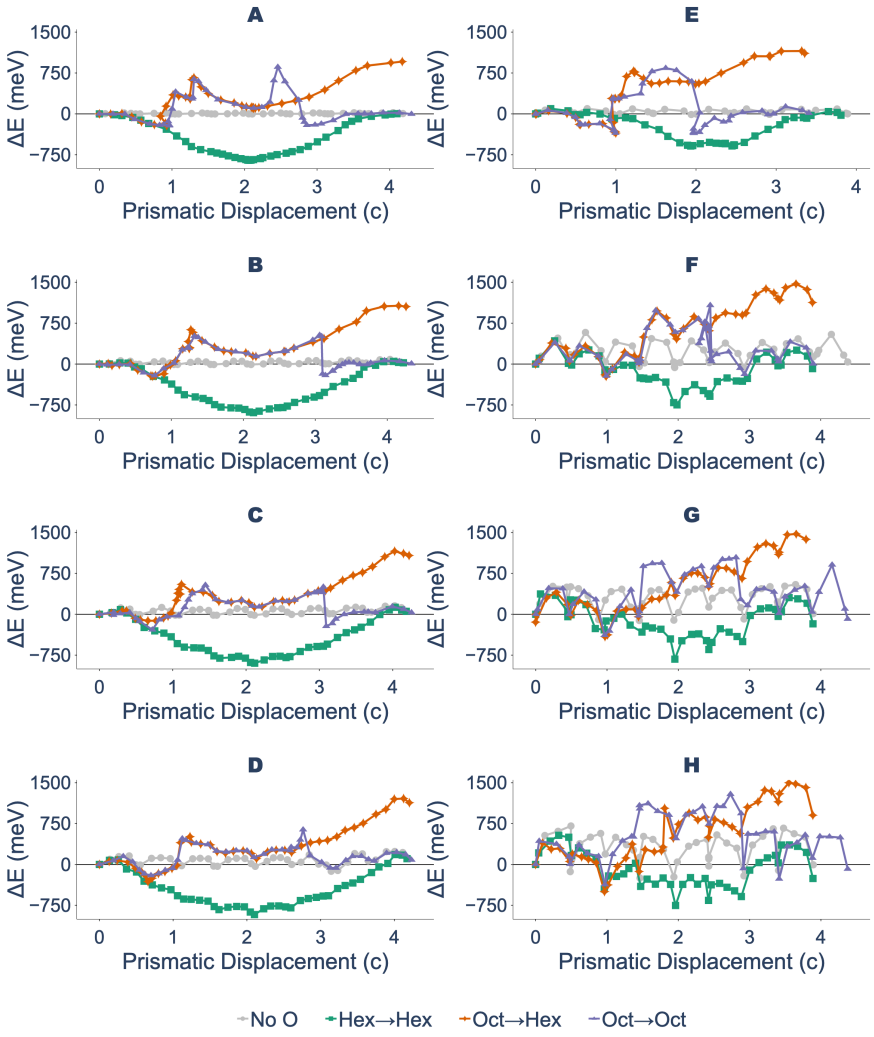

Figure 4.3: Relative energy along NEB pathway for 4 slip events with and without present interstitial atoms. A, B, C, and D are under no non-Schmid stress with simulation cells 3b, 15b, 30b, and 60b deep respectively. E, F, G, and H are under 3 GPa non-Schmid stress with simulation cells 3b, 15b, 30b, and 60b, respectively.

Because the interaction with the octahedral oxygen is a short-ranged contact interaction, it was expected to be unaffected by the added shear strain, whereas the barrier to motion from the long-ranged attraction to the oxygen in the hexahedral and core site was expected to be counteracted by the added shear.

The results shown in Fig. 4.5 show a pronounced barrier to return to the octahedral site for the prismatic core simulation. However in the pyramidal core simulation there is little to no barrier for return to the octahedral site, this suggests that interstitial shuffling is unlikely

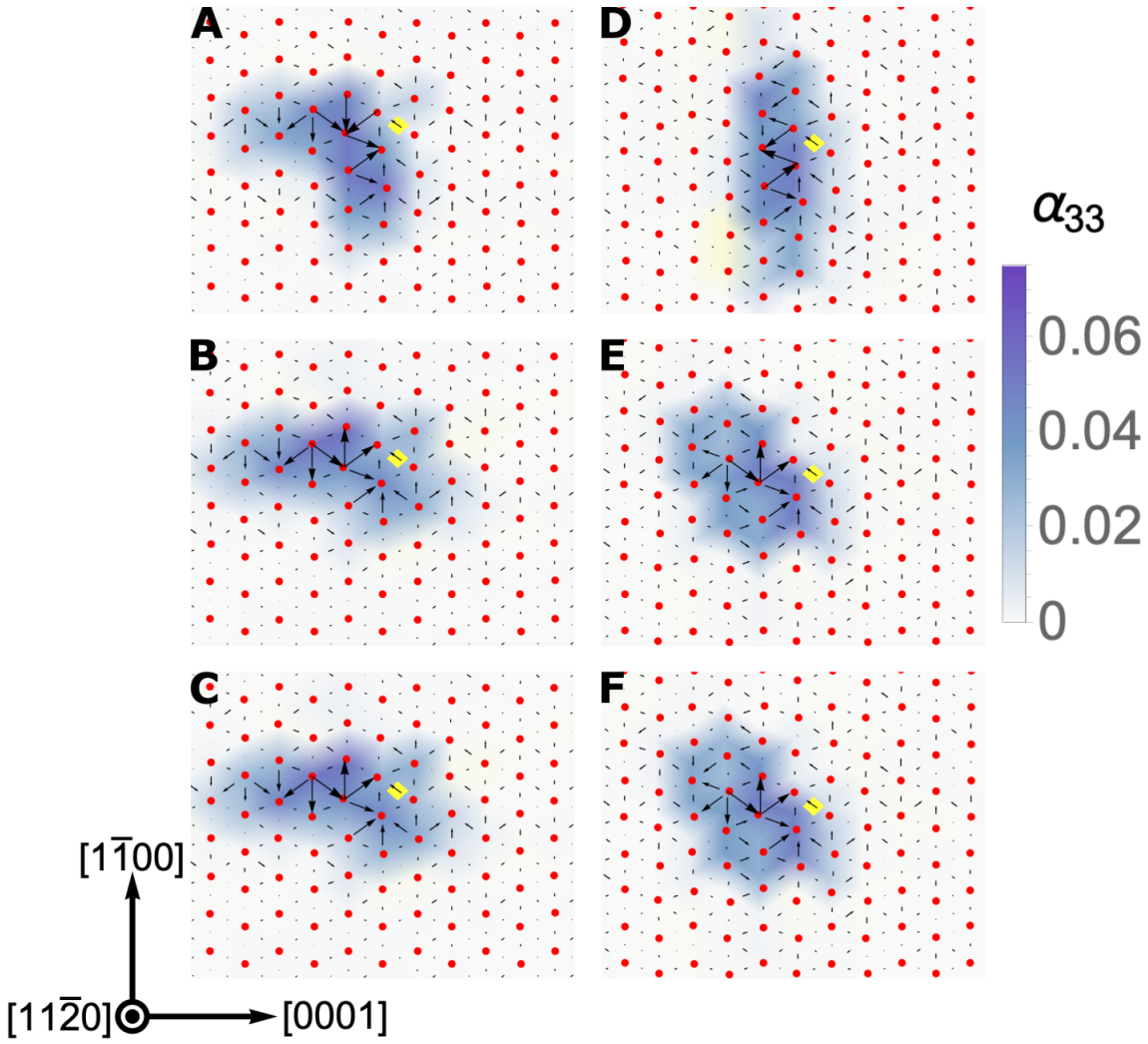

Figure 4.4: Nye tensor and Vitek maps of dislocation at lowest energy metastable core structure seen as the dislocation approaches the octahedral oxygen (where slip number=1 in Fig. 4.3). A-C show the unstressed core, for cells of 3, 15, and 30b thick respectively. D-F show the Schmid-stressed core for cells of 3, 15,and 30b respectively. The yellow diamond indicates the position of the oxygen atom.

to occur when the dislocation is pyramidally dissociated, or when it is compact when the oxygen is in the core interstitial site.

Micromechanics calculations

The long-ranged attractive interaction between hexahedral oxygen the prism core seems well predicted by the micromechanical calculation shown in Fig. 4.6. As seen in Table 4.1, our MEAM calculations show an attraction between the hexahedral oxygen and the dislocation with a strength of 1.04 eV (0.72 eV) for the prismatic (pyramidal) core. The micromechanical calculation here predicts the hexahedral interstitial has a -0.90 eV (-0.50 eV) attraction to a dislocation in the prismatic (pyramidal) configuration. The values for the prismatic core are in reasonable agreement with the MEAM calculation. For the pyramidal core, the larger energy between the MEAM and micromechanical calculation is unsurprising given the rearrangement in the core structures seen in Fig. 4.6.

Molecular Dynamics Simulations

In addition to the NEB simulations and micromechanics analysis, MD simulations of a dislocation slipping past an octahedral interstitial were performed to examine the possibility of interstitial shuffling at temperature (300K) and high strain rate. In these simulations the same supercell arrangement as the 15 b cells for NEB were used, but with one octahedral oxygen placed 2 c away from the left dislocation in the prism direction, and six oxygen placed 2 c from the right dislocation in the prism direction at the same "y" position as the dislocation and $\pm 1\langle 1\bar{1}00\rangle$ away from the dislocation evenly spaced along the dislocation line. This oxygen served to completely lock the right dislocation so that it did not affect the slip of the left dislocation.

After the cells were equilibrated with 1000 0.001 ps timesteps using a Nose-Hoover NPT thermostat (Hoover, 1985; Nosé, 1984a; Nosé, 1984b) and the Parinello Rahman method (Parrinello & Rahman, 1981), a constant engineering strain rate oriented for prism slip was applied. MD under applied strain rate used a NVT SLLOD thermostat (Edwards et al., 2006).

The results under various strain rates and non-Schmid stresses are summarized in Table 4.2:

$\dot{\epsilon}$	5×10^9	1×10^9	5×10^8	1×10^8
Prism Pyr	Shuffle Cross	Cross Cross	Shuffle Cross	Shuffle Cross

Table 4.2: Behavior (shuffle or cross slip) of dislocation encountering oxygen in MD simulations at various strain rates.

These results show that the dislocation shuffling an interstitial atom is a possible alternative to cross slip for the prismatic dislocation, and that the probability of shuffling may be reduced by application of non-Schmid stress. These results are rather limited as only

extremely high strain rates are examined due to computational limitations on simulation length (for reference, the highest strain rate simulation used in experiments in Ref. (Chong et al., 2020) was $10^3/s$), and only one simple arrangement of oxygen interstitials was used.

4.4 Discussion and Summary

The first result of this work is stronger evidence for the occurrence of interstitial shuffling of oxygen in α-Ti. Previous work claims interstitial shuffling could cause slip-plane softening, which is a precursor to brittle failure (Chong et al., 2020). Those results relied on GSF calculations as an argument for interstitial shuffling to occur. Using full dislocations instead of stacking faults removes arbitrary constraints on the motion of the interstitial as well as Ti atoms in the dislocation core. This in turn enables the interstitial atom to interact with the strain field around the dislocation.

The results presented here show that shuffling is likely to occur given a prismatically spread dislocation core, the preferred core strucure under no non-Schmid stress in the MEAM potential used. While the pyramidal core is favored in DFT simulations without oxygen present, the metastable prismatic core is expected when slip is occurring on the prismatic plane (Clouet et al., 2015).

However, the results presented here also show shuffling will be suppressed by an applied non-Schmid stress. Under non-Schmid stress, the core structure is altered to be more pyramidal, and remains relatively compact on the prismatic plane even when the dislocation is prismatically slipping. This shows that there is a significant effect of core structure on dislocation interstitial interaction.

The effect of core structure on the occurrence of shuffling is explained by the difference in attraction between the interstitial oxygen and the core fields of the two dislocation structures, calculated using micromechanics. While the strain field around an idealized screw dislocation is purely shear, and therefore would not be expected to interact with the interstitial atom, the core fields around the dislocations in these simulations have tensile components.

The connection between core structure and interstitial shuffling suggest that an alloy which strongly favors the pyramidal core over the prismatic core may have reduced susceptibility to oxygen embrittlement. This may help explain the experimentally observed reduction in oxygen sensitivity seen experimentally in experiments of Ti-xAl alloys (Chong et al., 2021). This correlates well with DFT simulations that have shown a propensity for basal and pyramidal spreading of the dislocation core, as well as an increase in the prismatic SFE (Kwasniak et al., 2016; Tsuru et al., 2022a). As there is interest in discovering more oxygen tolerant Ti alloys, simulation of dislocation core structure may be a useful step in alloy design.

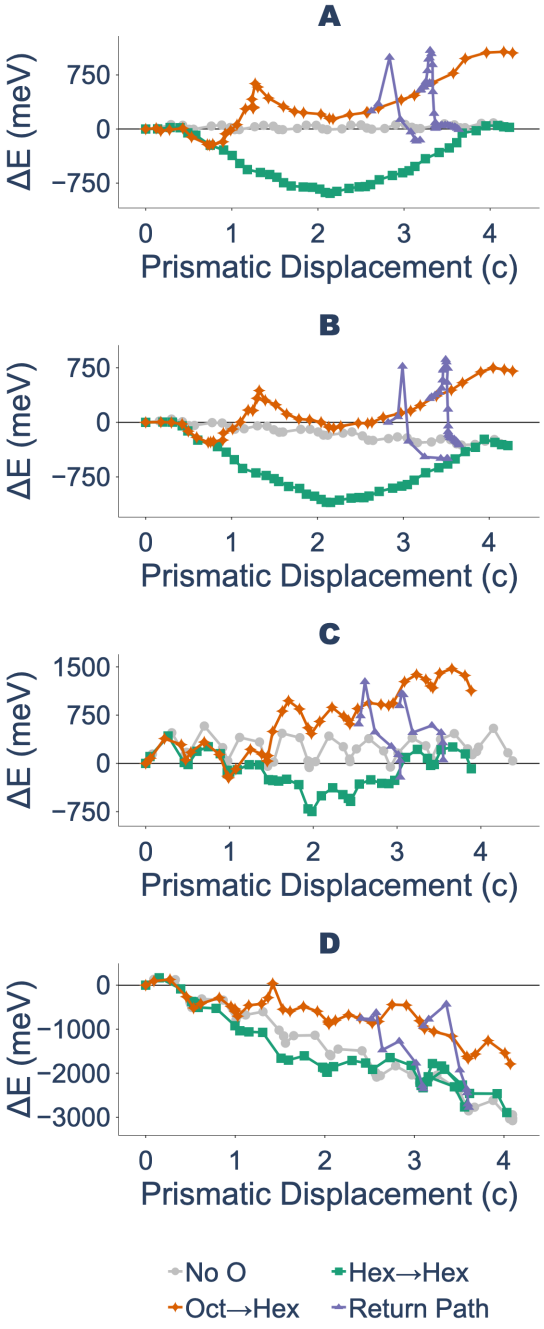

Figure 4.5: Relative energy along NEB pathway for 4 slip events with and without present interstitial atoms for the following cases: A no non-Schmid or Schmid stress, B no non-Schmid stress but shear stress of 20 MPa applied, C non-Schmid stressed but unsheared, D non-Schmid stressed and shear stress of 100 MPa applied.

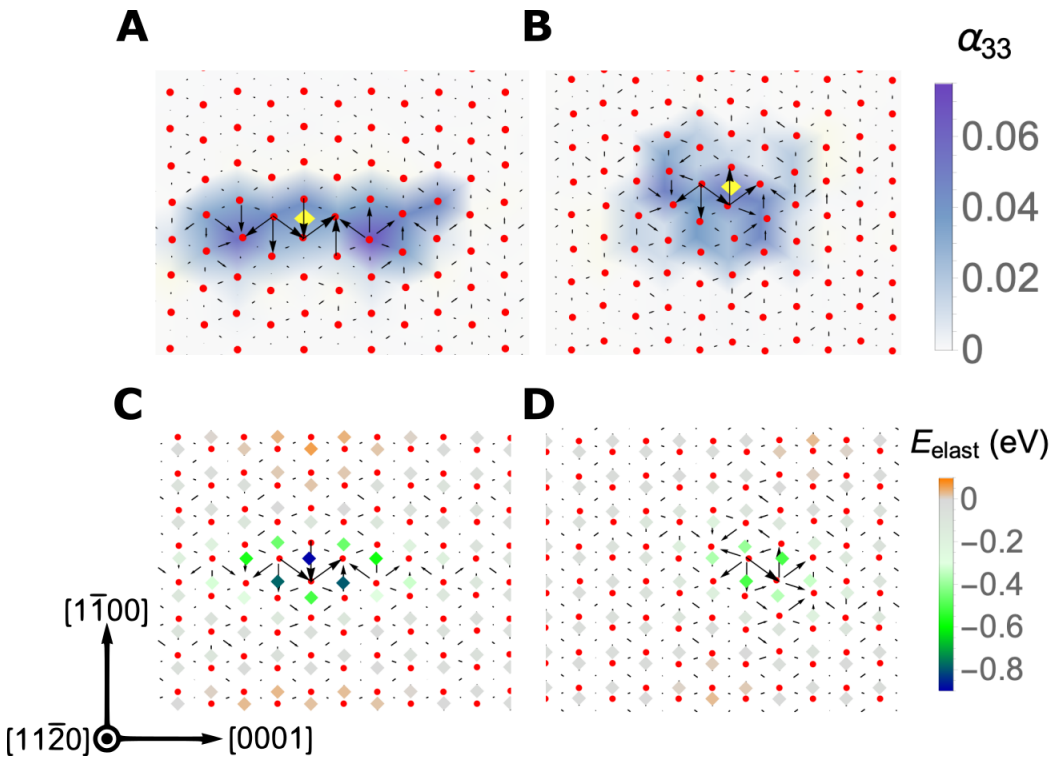

Figure 4.6: A and B show the spreading of the dislocation with the oxygen in the core interstitial site, A unstressed and B with non-Schmid stress applied. C and D show the calculated elastic interaction from 4.1, for prismatic core and hexahedral oxygen, and the pyramidal core and hexahedral oxygen respectively.

Chapter 5

Cottrell atmospheres around screw dislocations

5.1 Background

Cottrell atmospheres (Cottrell & Bilby, 1949), the collections of interstitial impurities that form around dislocations, are known to influence strongly the mechanical properties of metals. This atmosphere forms because solute atoms are attracted to the stress/strain field associated with a dislocation, and in effect cause the dislocation to become pinned. In the typical case, they occur with the interaction of a small interstitial impurity interacting with an edge dislocation in an face centered cubic or body centered cubic metal such as iron.

For the case of screw dislocations, linear elasticity theory predicts that there is no interaction between a screw dislocation (which, excluding the core region has a purely shear strain field) and an oxygen interstitial (whose elastic dipole tensor is purely dilational in character). In the case of HCP Ti there is, however, a short-ranged contact interaction (Chaari et al., 2019; Yu et al., 2015). The change in energy of a screw dislocation around a solute is then the sum of the effects of change of stacking fault energy, elastic interaction with the core field, and elastic interaction with the long-ranged field:

$$\Delta E_{dis} = \Delta E_{\Delta SFE} + \Delta E_{elastic-core} + \Delta E_{elastic-long} \tag{5.1}$$

The methods used in this study are intended to isolate the Cottrell atmosphere effect from the contact interaction.

As mentioned previously in this dissertation, studies of the $\langle a \rangle$-type screw dislocation cores show some degree of polymorphism, and that the dynamics of the dislocations are controlled by their core spreadings (Chrzan et al., 2022; Clouet et al., 2015; Poschmann et al., 2022). What follows is part of a simple analysis to show how the core spreading of an $\langle a \rangle$-type screw dislocation, which may be imagined as partial dislocations without stacking faults, can lead to substantial linear elastic interactions between the dislocation and the

oxygen interstitials, and how these elastic interactions may have profound consequences for the dislocation dynamics.

5.2 Dissociation Model

In the NEB studies of dislocation slip from the last chapter, some curious results were seen in regards to the structure of the dislocation as it approached the octahedral interstitial. As seen in Fig. 4.4 A and D, the dislocation takes on a basal, or non-planar arrangement at high oxygen concentrations along the dislocation line while the oxygen is at the edge of the core region. Analysis using the DXA algorithm in OVITO identifies Fig. 4.4D as a basally dissociated dislocation with partial Burger's vectors of $\frac{1}{3}\langle 10\bar{1}0\rangle$ and $\frac{1}{3}\langle 01\bar{1}0\rangle$. Fig. 4.4A is identified as a complex (threefold) splitting core with partial Burger's vectors of $\frac{1}{3}\langle 01\bar{1}0\rangle$, $\frac{1}{18}\langle 44\bar{0}3\rangle$, and $\frac{1}{18}\langle 24\bar{6}\bar{3}\rangle$.

It should be noted that the threefold core is essentially splitting the one of the two basal cores again.

$$\frac{1}{18}\langle 44\bar{0}3\rangle + \frac{1}{18}\langle 24\bar{6}\bar{3}\rangle = \frac{1}{3}\langle 10\bar{1}0\rangle \tag{5.2}$$

This dissociation clearly violates Frank's rule, that the sum of squared Burger's vectors of a dissociation should be lower than the squared Burger's vector of the undissociated dislocation in order for it to be energetically favorable. This is evidence that there must be some other energy in the balance here, and in the analysis here that energy is the elastic interaction energy between an interstitial atom and the dissociated partial dislocations.

In the molecular dynamics simulations below we see these same dissociations in random solute fields; in some cases there are discernible stacking faults between the partial dislocations and in other cases there is not a measurable stacking fault length. However, it still seems wise to first rule out a Suzuki segregation effect on the stacking faults when it does exist.

5.3 Methods

Calculation of interstitial attraction to basal stacking fault

In order to rule out Suzuki segregation as the source of core structure change, the energy of attraction of an oxygen interstitial to the basal stacking fault was performed. One interstitial oxygen was placed in a supercell with two basal stacking faults 30 stacking layers apart, leaving one oxygen per 24000 Ti atoms. The oxygen was placed in various layers and the supercell was relaxed with fixed (periodic) lattice vectors. The energy of segregation to the stacking fault was then the difference between the energy of the cell with the oxygen equidistant to the two stacking faults and the cell with oxygen 1 layer away from one stacking fault. The calculated attraction to the stacking fault was 2 meV/oxygen. Given a 1%

occupation of octahedral interstitial sites, this corresponds to a change in stacking fault energies of roughly 0.04mJ/m^2. Considering that the basal SFE of Ti is 170mJ/m^2 in MEAM and 300mJ/m^2 in DFT (Hennig et al., 2008), a decrease on the order of several hundredths of a percent is likely much too small to lead to the observed basal dissociation.

Molecular dynamics simulation of core structure in random environments

Compared to a reference prismatic core, in the absence of oxygen, the pyramidal dislocation core is favored by 3.67 meV/b, and the basal core is disfavored by 135 meV/b in the MEAM potential (Zhang & Trinkle, 2016).This was calculated by inserting 20*[0001] by 20*[1$\bar{1}$00] by n*[11$\bar{2}$0] cells using the BABEL code (Clouet, n.d.) with various initial positions of the elastic singularity. For the basal dislocation $\langle 1\bar{1}00\rangle$ partial dislocations were initially placed. The celled were then relaxed with conjugate gradient minimization in LAMMPS and resulting energies were compared. The energies are similar to values seen in DFT (Tsuru et al., 2022b). However, when oxygen atoms are introduced, the relative energies of the dislocation structures change significantly, even when the O atoms are placed outside of the dislocation core. To examine this behavior, a series of periodic supercells were created containing dislocation dipoles and a random arrangement of oxygen atoms. A screw dislocation dipole was inserted into 20*[0001] by 20*[1$\bar{1}$00] by n*[11$\bar{2}$0] cells using the BABEL code (Clouet, n.d.), with all octahedral interstitial sites filled with oxygen. Then 100 configurations for each length and oxygen concentration were generated by randomly removing oxygen until the desired at. % oxygen was reached. Then all oxygen within 4 A of the dislocation placement position was removed to minimize the contact interaction between the oxygen and the dislocation. Each cell underwent conjugate gradient minimization before 10 ps of molecular dynamics at 150K, and a 10ps cooling to 1K in an NVT ensemble using a Langevin thermostat (Dünweg & Paul, 1991; Schneider & Stoll, 1978). This calculation gives a prediction of dislocation dissociation as a dislocation moves through different environments at effectively 0 strain rate and mostly excludes the core-field interactions.

After MD simulations, the DXA algorithm in OVITO was used to identify the $\langle 1\bar{1}00\rangle$ (basal) splitting, or more complex (threefold, fourfold) splittings (Stukowski et al., 2012).

Molecular dynamics simulation of dislocation motion in a field of solutes

To test if the dislocation will dissociate when forced to move through a field of solutes at high strain rate, dislocations were introduced into cells 20*[0001] by 20*[1$\bar{1}$00] by 30*[11$\bar{2}$0] using the BABEL code (Clouet, n.d.). A constant engineering strain rate of $8 * 10^8/s$ oriented for prism slip was applied, while molecular dynamics was performed using a NVT SLLOD thermostat at 300K (Edwards et al., 2006). Once again the DXA algorithm was used to identify dislocation splitting. Here oxygen was not excluded from the dislocation core.

Calculation of elastic dipole tensor

Elastic dipole tensors (EDTs) were calculated using the residual stress method (Varvenne & Clouet, 2017). DFT calculations were performed using the Vienna *ab initio* Simulation Package (VASP) (Kresse & Furthmüller, 1996a, 1996b), using the projector augmented wave method(Blöchl, 1994; Kresse & Joubert, 1999) and a Perdew–Burke–Ernzerhof form functional (Perdew et al., 1996) including the 3p (Ti_pv). DFT calculations were converged with a cutoff energy of 1000 eV, a minimum of 35000 k points-per-reciprocal-atom, and a Methfessel-Paxton smearing (Methfessel & Paxton, 1989) of 0.05 eV. Several sizes of $n \times m \times l$ cells were considered, where n, m, and l refer to the number of repeats along the $\frac{1}{3}[1\bar{2}10]$, $[10\bar{1}0]$, and $[0001]$ directions respectively. The reported values of $P11$ and $P33$ were the average of the values from the $4 \times 2 \times 2$, $3 \times 3 \times 2$, and $3 \times 2 \times 3$ cells. The average differed by less than 2% from the values from the $3 \times 2 \times 2$ cell. The calculated elastic dipole tensor for an octahedral oxygen using the residual stress method in DFT was (in eV):

$$P_{oct} = \begin{bmatrix} 2.35 & 0 & 0 \\ 0 & 2.35 & 0 \\ 0 & 0 & 3.96 \end{bmatrix}. \tag{5.3}$$

Calculation of elastic fields of attraction

To calculate the elastic fields around an infinite straight dislocation in anisotropic linear elasticity theory, the equations of Stroh's sextic formalism (Stroh, 1958) are used. In Stroh's formalism, the assumed form of the displacement field ($u(x_1, x_2)$) is:

$$u_k = A_k f(x_1 + p x_2) \tag{5.4}$$

Where f is an analytic function of a complex variable, and A_k is a constant vector (implying that the displacement is not a function of the third direction x_3). This is considered a valid assumption in the case of an infinite straight dislocation when x_3 is the dislocation line direction. A_k will then be in the Burger's vector direction.

After calculating the stress field around a dislocation, using Stroh's solution, the stress around the dislocation is translated into strain field around the dislocation using Hooke's Law.

$$\epsilon_{ij} = S_{ijkl} \tau_{kl} \tag{5.5}$$

Where $\mathbf{S}$ is the compliance tensor (from the inverted elastic constants) and η is the strain. The elastic constants used in this section for HCP Ti are:

$$C_{11} = 174$$
$$C_{12} = 95$$
$$C_{13} = 72$$
$$C_{33} = 188$$
$$C_{44} = 58.0$$

Because linear elasticity it assumed, the strain fields of two or more partial dislocations may simply be added to calculate the strain field of the whole dislocation. The interaction energy between the interstitial and these summed strain fields is simply calculated using Eq. 4.1.

5.4 Results

Low energy structures in random environments

The low energy structures in random environments with oxygen excluded from the dislocation core also showed significant amounts of kink formation. These results are shown in Fig. 5.1. In the analysed cases, DXA identifies partial dislocations that have not spread far enough to have a recognizable stacking fault as well as partial dislocations that have fully separated. Often, the splitting does not extend the whole length of the dislocation (see Fig. 5.1), suggesting that local fluctuation in the environment around the dislocation can lead to this splitting. It is noted that an increase in the oxygen content clearly leads to an increase in the amount of splitting observed.

Since the oxygen has been excluded from the region around the initial placement of the dislocation (although there are some cases where the dislocations have migrated towards the oxygen), this appears to be a long-ranged effect as opposed to the elastic interaction with the dislocation core field discussed in the last chapter. It will be necessary in the future to compare this to the amount of splitting predicted by the linear elastic model with micromechanical interaction.

Molecular dynamics of dislocation motion

Dislocations moving through a field of random solutes at high strain rates also show basal and three-fold dissociation. These results corroborate the observations obtained from the simulations of low energy structures in random environments.

The presence of oxygen is shown to increase the amount of the dislocation that is dissociated on average, especially under applied non-Schmid stress. The results are summarized in Fig. 5.2. Notably, the dislocations in the presence of oxygen have at least one kink pair at almost all timesteps. Here, the term kink is used to describe any time the dislocation

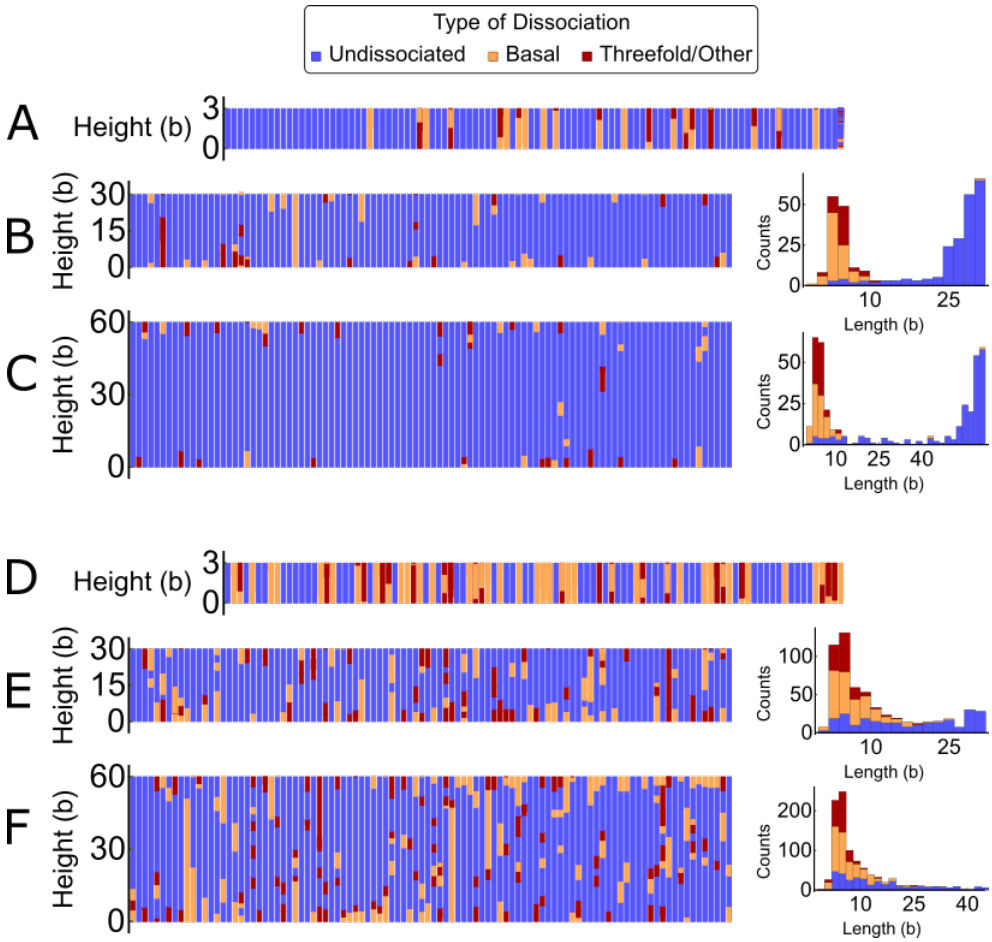

Figure 5.1: (left) Schematic of DXA results along the length of the left dislocation for each sample, each bar represents a different sample and the type of dissociation along the height of the cell is represented by color. (right) stacked histogram of lengths of segments for both dislocations in all 100 random cells colored by type of dissociation. A-C are 1 at. % oxygen for 3, 30, and 60 b cells respectively. D-F is the same for 3 at. % oxygen. Histograms for 3 b cases excluded.

forms a segment that is differently dissociated than the other segments around it, i.e. a basal segment is formed in an otherwise undissociated dislocation. The dissociated structures are generally either basal or a more complex 3-fold dissociation, although sometimes take other structures. Because of the high strain rate of these simulations, a significant amount of debris was created during the the deformation process. Oxygen shuffling into the hexahedral site was also observed. Also important to note is that oxygen was not excluded from the dislocation core in this simulation, so it is hard to separate core-field and long-ranged effects.

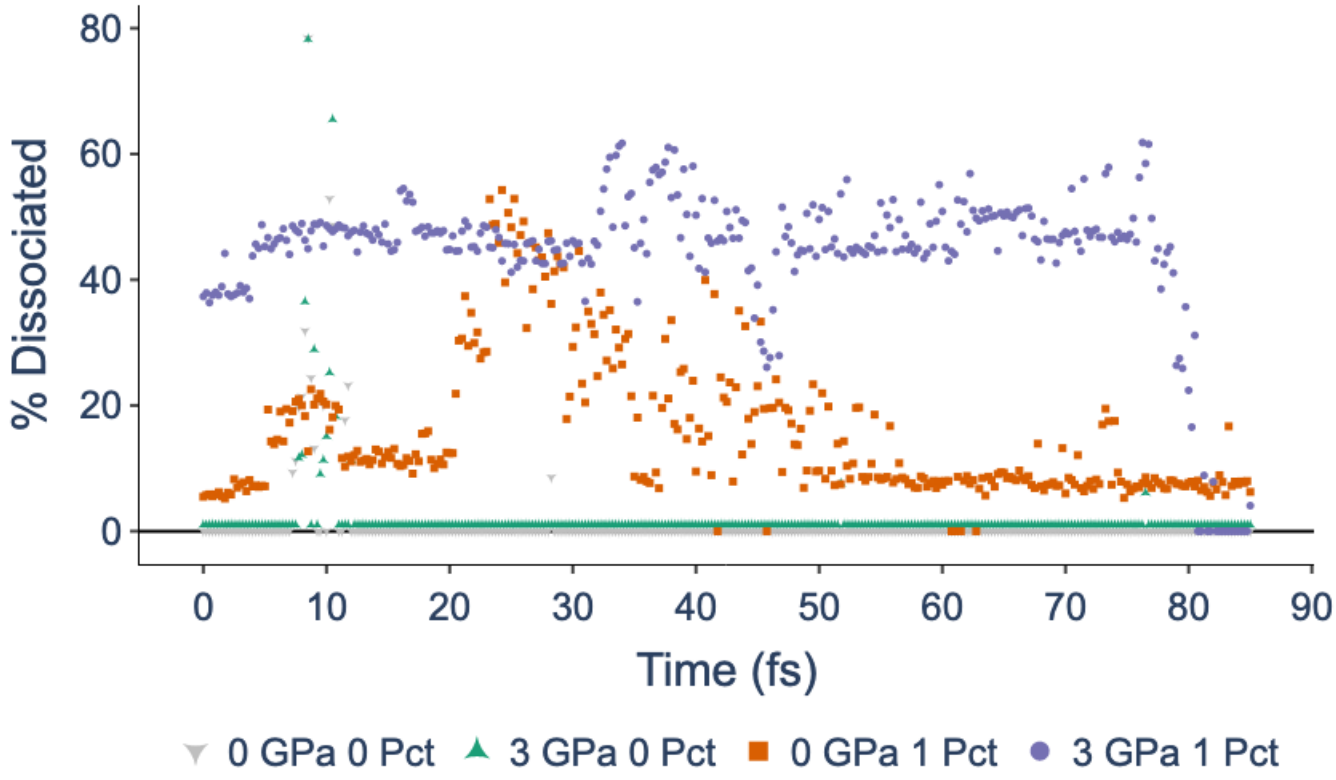

Figure 5.2: The percent of length of the dislocation line that is dissociated is displayed at each time-step as a pair of dislocations are sheared through a field of oxygen solutes. The cases are with and without non-Schmid stress, and with and without 1 at. % oxygen. The 3GPa 0 pct. line has been shifted up by 1 percent on the y-axis to not overlap with the 0GPA 0 Pct line.

Long-ranged elastic interaction from Stroh theory

The results of an example calculation of the long-ranged elastic interaction from Stroh theory and Eq. 4.1 using the DFT calculated elastic dipole tensors for the basal and threefold dislocation are displayed in Figs. 5.3 and 5.4.

Notably, for the case of a basal dissociated dislocation, the field of interaction energy is symmetric. This means that in the limit of an infinitely long, straight dislocation, there is no expected energy change from the introduction of a field of solutes. However, as a real dislocation may kink, we can expect some fluctuation of the core structure along the

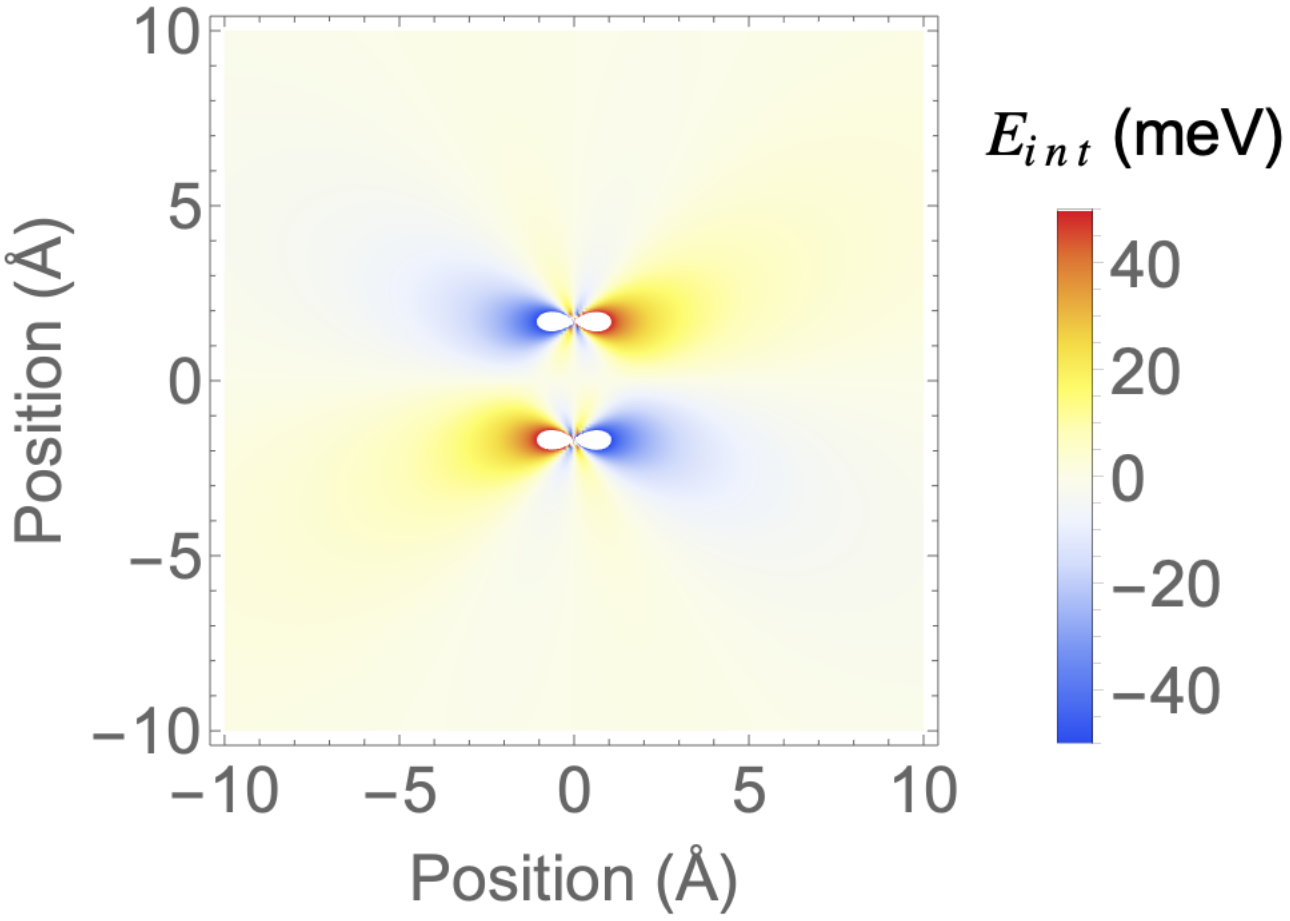

Figure 5.3: Interaction energy between an oxygen interstitial and an infinite straight pair of $\langle 1\bar{1}00 \rangle$ partial dislocations. Plot coloring clips to white when out of -50 to 50 meV range.

dislocation line to minimize the energy of the dislocation-solute system. This explains the frequent kink formation (using the term kink as earlier) from both sets of molecular dynamics simulations.

This symmetry in interaction energy should be true for any pair of edge partials, and since in linear elasticity theory strain fields may be summed, the argument of this effect only causing local changes in energy along the dislocation line should hold true for the threefold dissociated case as well. In this threefold case the interaction energy with the oxygen is much higher at some positions than with the basal dissociated case, which may explain the violation of Frank's rule for dislocation dissociation.

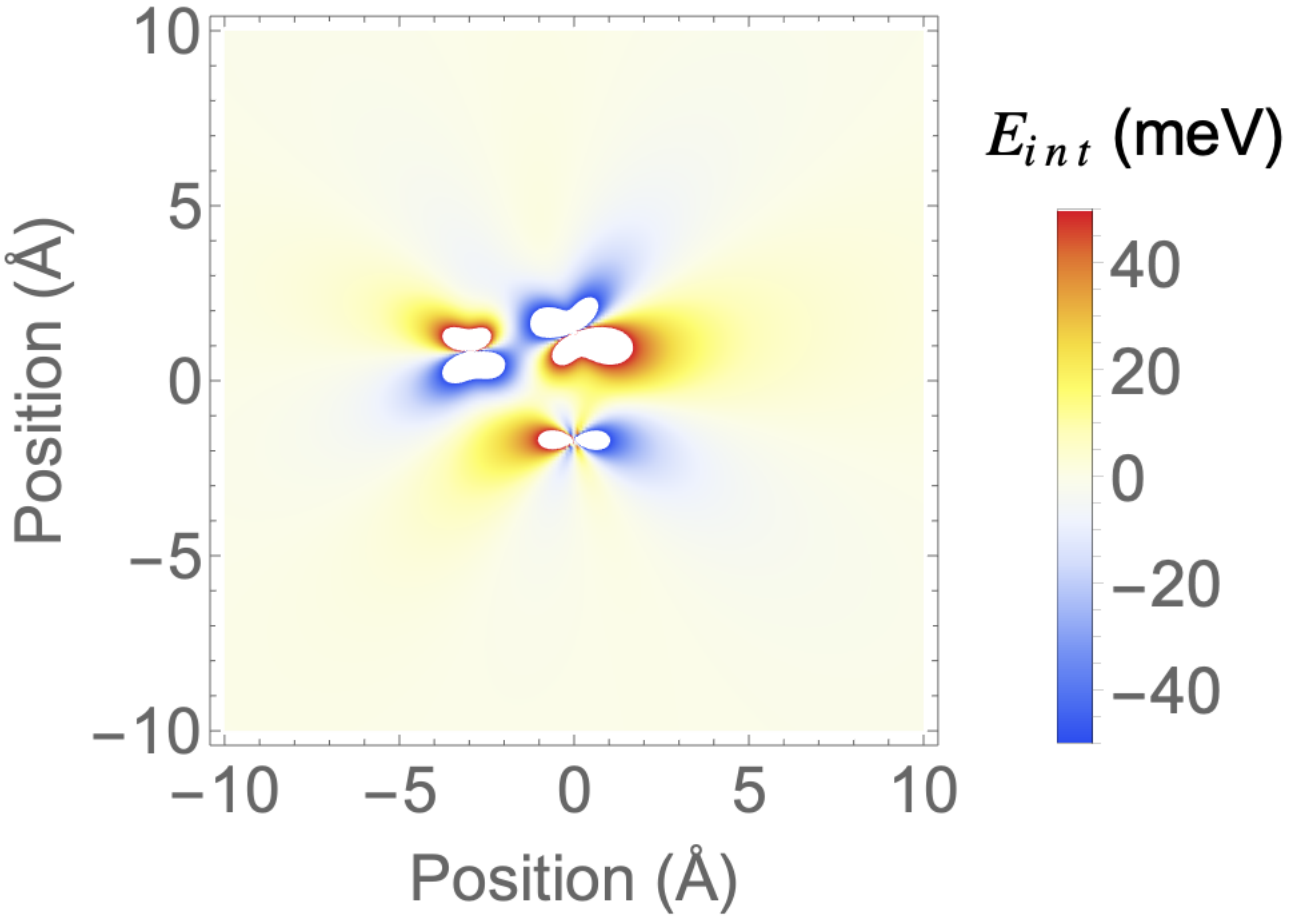

Figure 5.4: Interaction energy between an oxygen interstitial and an infinite straight threefold dissociated dislocation. Plot coloring clips to white when out of -50 to 50 meV range.

5.5 Discussion

The results in this chapter show how oxygen outside of the core region can still locally change the relative energies of dislocation core structures. This is meaningful for a few reasons. The first, is that this may affect dislocation dynamics, especially with high concentrations of solute atoms. For example, solute atoms may be nucleation sites for the dislocation to kink into a different core structure and then cross-slip. Or, local cross-slip and jog formation may be encouraged. Secondly, local fluctuations should act as a source of strengthening. Small segments of dislocations stuck in core configurations where slip is not favorable may pin larger segments of a dislocation in place, increasing the yield strength of a material. This effect may be related to the effects seen in simulations by Li *et. al* (Q.-J. Li et al., 2019), who observed dislocation roughening influenced by chemical short-ranged ordering

in the NiCoCr medium entropy alloy. High entropy and medium entropy alloys have often been shown to have high yield strengths. Finally, in the case of Ti, the ISM may be locally discouraged by changing the dislocation core structure, so if an alloying element that has the same effect as oxygen in terms of creating local fluctuations along the dislocation line was added to a Ti-O alloy it may serve to reduce some of oxygen's embrittling effects. Developing an understanding of the relative energies of the various effects on dislocation core structure energy (as described in Eqn. 5.1) gives an engineer a pathway towards designing an alloy to have certain dislocation core structures and therefore dynamics.

Chapter 6

Outlook and Suggested Future Work

6.1 Outlook

It has been shown in MEAM simulations that core structure affects the likelihood of interstitial shuffling. This increased understanding of the interstitial shuffling mechanism gives motivation for engineering the $\langle a \rangle$-type screw dislocation core structure in Ti to more favor the pyramidal core compared to the prism core.

A better understanding of the core field and Cottrell atmosphere elastic interactions with dislocations have provided more ways to change the dislocation core structure than the traditionally discussed stacking fault energy and Suzuki segregation effects. This local affect is theorized to affect dislocation dynamics and the material's yield strength. It is hoped that these understandings could lead to more informed computational design of Ti alloys and other materials.

6.2 Suggestions for Future Work

Ti-Al-O Alloys

Chong *et. al* showed that Al, when added to a Ti-O alloy, can increase both strength and ductility of said alloy (Chong et al., 2021). In their study, alloys with increased ductility exhibited more strain delocalization, with dislocation entanglements and cross-slips between planar slip bands. They also claim that the ISM is likely impeded by the high energy of Al-O bonds that would be introduced by shuffling.

This synergistic behavior between aluminum and oxygen also agrees with the analysis here that shows the ISM is dependant on dislocation core structure. Kwasniak *et. al* showed that Al increases the prismatic SFE and decreases the basal SFE (Kwasniak et al., 2016). This should increase the probability of cross-slip, instead of shuffling, as the dislocation may take a pyramidal or basal structure as it approaches the dislocation. Also, Al in the Ti

matrix should cause local fluctuations along the dislocation line. Using the same method as in Ch. 5 for calculating the elastic dipole tensor of Al gives the result (in eV):

$$P_{Al} = -\begin{bmatrix} 1.14 & 0 & 0 \\ 0 & 1.14 & 0 \\ 0 & 0 & 1.80 \end{bmatrix} \tag{6.1}$$

This elastic dipole tensor is on the same order of magnitude as that for oxygen in Ti, but Al as a substitutional solute could be at up to 10 at. %. How that affects the amount and type of local fluctuations along the dislocation line is yet to be understood.

Relative energies of the different effects

Throughout this dissertation it has been shown how dislocation core structures in Ti can be changed by interactions with interstitial atoms. As suggested above in the case of Al, the cores structures will also be changed by substitutional atoms through the same effects (core field, SFE, Suzuki segregation, and our newly introduced screw dislocation Cottrell effect). In order to engineer desired slip behavior, an understanding of the relative energies of each of these effects is needed.

In Ch. 5 there a method is shown to separate core-field and long-range elastic effects based on placement of the solute atoms with respect to the dislocation in initial configurations. Separating these effects from the change in elastic constants and GSFE will take some more work. One suggested way to study the relative energies of these effects would be to find a model system with an empirical potential where a solute minimally changes stacking fault energies while still acting as a point source of dilation. The Ti-Zr alloy system is a likely candidate for these tests.

Core structure predictions

While the previously suggested study would help better predict how elastic dislocation-solute effects change the relative energy of dislocation core structures, they would not give an initial prediction of said relative energies. One possible way to perform that prediction would be to use the semidiscrete variational Peierls Nabarro model (SVPN).

The SVPN model, devised for prediction of Peierls barriers, describes the energy of a dislocation as follows (Bulatov & Kaxiras, 1997; Lu et al., 2000a, 2000b)

$$U_{dis} = U_{elastic} + U_{misfit} + U_{stress} \tag{6.2}$$

where $U_{elastic}$ has a configuration-independent term associated with the long-range strain field, and a configuration dependant term. U_{misfit} is the energy from the disregistry at the interface of the two elastic half-spaces where the dislocation is located. For our purposes this will be the result of GSFE calculation. U_{stress} is the energy from an externally applied stress.

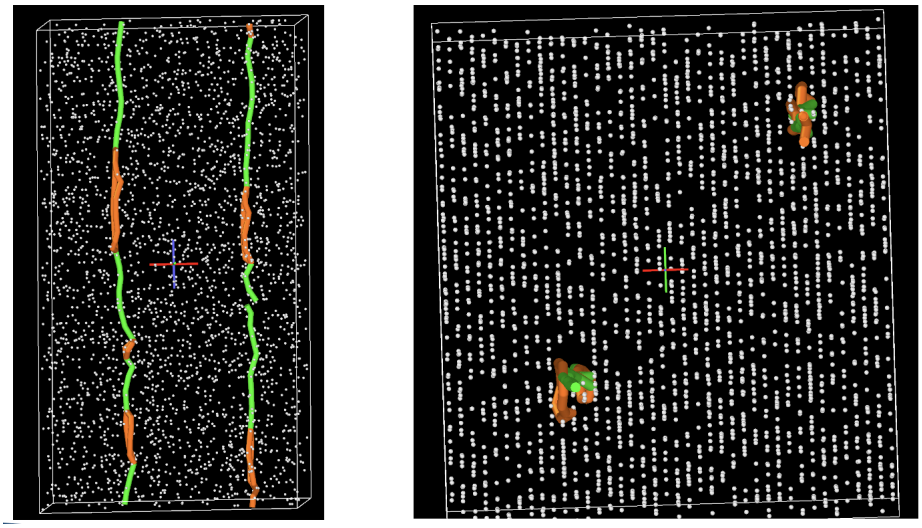

Figure 6.1: Side (left) and top-down (right) view of a dislocation in a random oxygen environment. Green lines are undissociated dislocation, and orange lines are basally dissociated as identified by OVITO's DXA modifier.

After the assumption of an initial disregistry function, the energy is minimized with a variational approach to find the extent of spreading of a dislocation in a certain plane and the associated energy. To find a Peierl's barrier an external stress is applied until the dislocation is found to move. Some initial attempts to used the SVPN to predict the relative energies of the prism, pyramidal, and basal cores have been unsuccessful, but there are a number of correction terms to the model that could potentially improve predictions.

Strengthening from local fluctuations

The last suggested direction for future work is to try to understand how local fluctuations affect the strength and ductility of a material. As seen in Fig. 6.1, small sections of dislocation may become basally dissociated. This should correspond to a large increase in the energy barrier for prismatic motion, as the dislocation usually has to rearrange to be spread on the appropriate plane before it slips.

Varvenne *et al.* (Varvenne et al., 2016) have introduced a model for strengthening in FCC high entropy alloys based on wavy motion of a dislocation through a varying potential energy landscape. It may be possible to adapt this to the HCP case, using energies from computed elastic interactions to understand the complex potential energy surface the dislocation moves through.

Bibliography

Bai, L., & Breen, D. (2008). Calculating Center of Mass in an Unbounded 2D Environment. *Journal of Graphics Tools*, *13*(4), 53–60. https://doi.org/10.1080/2151237X.2008.10129266

Banerjee, D., & Williams, J. (2013). Perspectives on titanium science and technology. *Acta Materialia*, *61*(3), 844–879. https://doi.org/10.1016/j.actamat.2012.10.043

Baskes, M. I. (1992). Modified embedded-atom potentials for cubic materials and impurities. *Physical Review B*, *46*(5), 2727–2742. https://doi.org/10.1103/PhysRevB.46.2727

Blöchl, P. E. (1994). Projector augmented-wave method. *Physical Review B*, *50*(24), 17953–17979. https://doi.org/10.1103/PhysRevB.50.17953

Bulatov, V. V., & Kaxiras, E. (1997). Semidiscrete Variational Peierls Framework for Dislocation Core Properties. *Physical Review Letters*, *78*(22), 4221–4224. https://doi.org/10.1103/PhysRevLett.78.4221

Chaari, N., Rodney, D., & Clouet, E. (2019). Oxygen-dislocation interaction in titanium from first principles. *Scripta Materialia*, *162*, 200–203. https://doi.org/10.1016/j.scriptamat.2018.11.025

Chong, Y., Poschmann, M., Zhang, R., Zhao, S., Hooshmand, M. S., Rothchild, E., Olmsted, D. L., Morris, J. W., Chrzan, D. C., Asta, M., & Minor, A. M. (2020). Mechanistic basis of oxygen sensitivity in titanium. *Science Advances*, *6*(43), 1–11. https://doi.org/10.1126/sciadv.abc4060

Chong, Y., Zhang, R., Hooshmand, M. S., Zhao, S., Chrzan, D. C., Asta, M., Morris, J. W., & Minor, A. M. (2021). Elimination of oxygen sensitivity in α-titanium by substitutional alloying with Al. *Nature Communications*, *12*(1), 6158. https://doi.org/10.1038/s41467-021-26374-w

Chrzan, D. C., Poschmann, M., Winter, I. S., & Asta, M. (2022). Thermodynamic model for polymorphic dislocation core spreading within hexagonal close packed metals. *Physical Review Materials*, *6*(1), 013604. https://doi.org/10.1103/PhysRevMaterials.6.013604

Chrzan, D. C., Sherburne, M. P., Hanlumyuang, Y., Li, T., & Morris, J. W. (2010). Spreading of dislocation cores in elastically anisotropic body-centered-cubic materials: The case of gum metal. *Phys. Rev. B*, *82*, 184202. https://doi.org/10.1103/PhysRevB.82.184202

Clayton, J. D. (2011). *Nonlinear mechanics of crystals*. Springer.

Clouet, E. (n.d.). *Babel*.

Clouet, E. (2012). Screw dislocation in zirconium: An *ab initio* study. *Physical Review B*, *86*(14), 144104. https://doi.org/10.1103/PhysRevB.86.144104

Clouet, E., Caillard, D., Chaari, N., Onimus, F., & Rodney, D. (2015). Dislocation locking versus easy glide in titanium and zirconium. *Nature Materials*, *14*(9), 931–936. https://doi.org/10.1038/nmat4340

Clouet, E., Ventelon, L., & Willaime, F. (2009). Dislocation core energies and core fields from first principles. *Physical Review Letters*, *102*(5), 1–4. https://doi.org/10.1103/PhysRevLett.102.055502

Conrad, H. (1981). Effect of interstitial solutes on the strength and ductility of titanium. *Progress in Materials Science*, *26*(2-4), 123–403. https://doi.org/10.1016/0079-6425(81)90001-3

Cottrell, A. H., & Bilby, B. A. (1949). Dislocation theory of yielding and strain ageing of iron. *Proceedings of the Physical Society. Section A*, *62*(1), 49–62. https://doi.org/10.1088/0370-1298/62/1/308

Crecy, A. d., Bourret, A., Naka, S., & Lasalmonie, A. (1983). High resolution determination of the core structure of 1/3⟨11 2 0⟩ 10 1 0 edge dislocation in titanium. *Philosophical Magazine A*, *47*(2), 245–254. https://doi.org/10.1080/01418618308245221

Daw, M. S. (2006). Elasticity effects in electronic structure calculations with periodic boundary conditions. *Computational Materials Science*, *38*(2), 293–297. https://doi.org/10.1016/j.commatsci.2006.02.009

Daw, M. S., & Baskes, M. I. (1984). Embedded-atom method: Derivation and application to impurities, surfaces, and other defects in metals. *Physical Review B*, *29*(12), 6443–6453. https://doi.org/10.1103/PhysRevB.29.6443

Daw, M. S., Foiles, S. M., & Baskes, M. I. (1993). The embedded-atom method: A review of theory and applications. *Materials Science Reports*, *9*(7–8), 251–310. https://doi.org/10.1016/0920-2307(93)90001-U

Dünweg, B., & Paul, W. (1991). Brownian dynamics simulations without gaussian random numbers. *International Journal of Modern Physics C*, *02*(03), 817–827. https://doi.org/10.1142/S0129183191001037

Edwards, B. J., Baig, C., & Keffer, D. J. (2006). A validation of the p-sllod equations of motion for homogeneous steady-state flows. *The Journal of Chemical Physics*, *124*(19), 194104. https://doi.org/10.1063/1.2192776

Falk, M. L., & Langer, J. S. (1998a). Dynamics of viscoplastic deformation in amorphous solids. *Phys. Rev. E*, *57*, 7192–7205. https://doi.org/10.1103/PhysRevE.57.7192

Falk, M. L., & Langer, J. S. (1998b). Dynamics of viscoplastic deformation in amorphous solids. *Physical Review E*, *57*(6), 7192–7205. https://doi.org/10.1103/PhysRevE.57.7192

Gerold, V., & Karnthaler, H. P. (1989). On the origin of planar slip in f.c.c. alloys. *Acta Metallurgica*, *37*(8), 2177–2183. https://doi.org/10.1016/0001-6160(89)90143-0

Gröger, R., & Vitek, V. (2012). Constrained nudged elastic band calculation of the Peierls barrier with atomic relaxations. *Modelling and Simulation in Materials Science and Engineering*, *20*(3), 035019. https://doi.org/10.1088/0965-0393/20/3/035019

Hartley, C. S., & Mishin, Y. (2005). Representation of dislocation cores using nye tensor distributions. *Materials Science and Engineering: A*, *400–401*, 18–21. https://doi.org/10.1016/j.msea.2005.03.076

Hayward, E., Deo, C., Uberuaga, B. P., & Tomé, C. N. (2012). The interaction of a screw dislocation with point defects in bcc iron. *Philosophical Magazine*, *92*(22), 2759–2778. https://doi.org/10.1080/14786435.2012.674646

Henkelman, G., & Jónsson, H. (2000). Improved tangent estimate in the nudged elastic band method for finding minimum energy paths and saddle points. *Journal of Chemical Physics*, *113*(22), 9978–9985. https://doi.org/10.1063/1.1323224

Henkelman, G., Uberuaga, B. P., & Jónsson, H. (2000). Climbing image nudged elastic band method for finding saddle points and minimum energy paths. *Journal of Chemical Physics*, *113*(22), 9901–9904. https://doi.org/10.1063/1.1329672

Hennig, R. G., Lenosky, T. J., Trinkle, D. R., Rudin, S. P., & Wilkins, J. W. (2008). Classical potential describes martensitic phase transformations between the , , and titanium phases. *Physical Review B*, *78*(5), 054121. https://doi.org/10.1103/PhysRevB.78.054121

Hohenberg, P., & Kohn, W. (1964). Inhomogeneous electron gas. *Physical Review*, *136*(3B), B864–B871. https://doi.org/10.1103/PhysRev.136.B864

Hoover, W. G. (1985). Canonical dynamics: Equilibrium phase-space distributions. *Physical Review A*, *31*(3), 1695–1697. https://doi.org/10.1103/PhysRevA.31.1695

Hurless, B., & Froes, F. (2002). Lowering the cost of titanium. *AMPTIAC Quarterly*, *6*(2), 3–9.

Jaffee, R. (1950). Alloys of Titanium With Carbon Nitrogen And Oxygen. *JOM*, *2*, 1261–1266.

Jaffee, R. I., Ogden, H. R., & Maykuth, D. J. (1950). Alloys of titanium with carbon, oxygen, and nitrogen. *JOM*, *2*(10), 1261–1266. https://doi.org/10.1007/bf03399142

Kelchner, C. L., Plimpton, S. J., & Hamilton, J. C. (1998). Dislocation nucleation and defect structure during surface indentation. *Physical Review B*, *58*(17), 11085–11088. https://doi.org/10.1103/PhysRevB.58.11085

Koss, D., & Chan, K. (1980). Fracture along planar slip bands. *Acta Metallurgica*, *28*(9), 1245–1252. https://doi.org/10.1016/0001-6160(80)90080-2

Kresse, G., & Furthmüller, J. (1996a). Efficiency of ab-initio total energy calculations for metals and semiconductors using a plane-wave basis set. *Computational Materials Science*, *6*(1), 15–50. https://doi.org/10.1016/0927-0256(96)00008-0

Kresse, G., & Furthmüller, J. (1996b). Efficient iterative schemes for ab initio total-energy calculations using a plane-wave basis set. *Physical Review B*, *54*(16), 11169–11186. https://doi.org/10.1103/PhysRevB.54.11169

Kresse, G., & Joubert, D. (1999). From ultrasoft pseudopotentials to the projector augmented-wave method. *Physical Review B*, *59*(3), 1758–1775. https://doi.org/10.1103/PhysRevB.59.1758

Kwasniak, P., Garbacz, H., & Kurzydlowski, K. J. (2016). Solid solution strengthening of hexagonal titanium alloys: Restoring forces and stacking faults calculated from first principles. *Acta Materialia*, *102*(January), 304–314. https://doi.org/10.1016/j.actamat.2015.09.041

Lehto, N., & Öberg, S. (1998). Effects of dislocation interactions: Application to the period-doubled core of the 90° partial in silicon. *Physical Review Letters*, *80*(25), 5568–5571. https://doi.org/10.1103/PhysRevLett.80.5568

Li, J., & Shimizu, F. (2005). Least-Square Atomic Strain.

Li, Q.-J., Sheng, H., & Ma, E. (2019). Strengthening in multi-principal element alloys with local-chemical-order roughened dislocation pathways. *Nature Communications*, *10*(1), 3563. https://doi.org/10.1038/s41467-019-11464-7

Lu, G., Kioussis, N., Bulatov, V. V., & Kaxiras, E. (2000a). Generalized-stacking-fault energy surface and dislocation properties of aluminum. *Physical Review B*, *62*(5), 3099–3108. https://doi.org/10.1103/PhysRevB.62.3099

Lu, G., Kioussis, N., Bulatov, V. V., & Kaxiras, E. (2000b). The Peierls-Nabarro model revisited. *Philosophical Magazine Letters*, *80*(10), 675–682. https://doi.org/10.1080/09500830050143778

Lütjering, G., & Williams, J. C. (2007). *Titanium* (2nd ed). Springer.

Maras, E., Trushin, O., Stukowski, A., Ala-Nissila, T., & Jónsson, H. (2016). Global transition path search for dislocation formation in Ge on Si(001). *Computer Physics Communications*, *205*, 13–21. https://doi.org/10.1016/j.cpc.2016.04.001

Methfessel, M., & Paxton, A. T. (1989). High-precision sampling for brillouin-zone integration in metals. *Physical Review B*, *40*(6), 3616–3621. https://doi.org/10.1103/PhysRevB.40.3616

Morris Jr, W., & Krenn, C. R. (2000). The internal stability of an elastic solid. *Philos. Mag. A*, *80*(12), 2827–2840. https://doi.org/10.1080/01418610030001257l

Naka, S., Lasalmonie, A., Costa, P., & Kubin, L. P. (1988). The low-temperature plastic deformation of -titanium and the core structure of a-type screw dislocations. *Philosophical Magazine A*, *57*(5), 717–740. https://doi.org/10.1080/01418618808209916

Nakano, A. (2008). A space-time-ensemble parallel nudged elastic band algorithm for molecular kinetics simulation. *Computer Physics Communications*, *178*(4), 280–289. https://doi.org/10.1016/j.cpc.2007.09.011

Nosé, S. (1984a). A molecular dynamics method for simulations in the canonical ensemble. *Molecular Physics*, *52*(2), 255–268. https://doi.org/10.1080/00268978400101201

Nosé, S. (1984b). A unified formulation of the constant temperature molecular dynamics methods. *The Journal of Chemical Physics*, *81*(1), 511–519. https://doi.org/10.1063/1.447334

Parrinello, M., & Rahman, A. (1981). Polymorphic transitions in single crystals: A new molecular dynamics method. *Journal of Applied Physics*, *52*(12), 7182–7190. https://doi.org/10.1063/1.328693

Perdew, J. P., Burke, K., & Ernzerhof, M. (1996). Generalized gradient approximation made simple. *Physical Review Letters*, *77*(18), 3865–3868. https://doi.org/10.1103/PhysRevLett.77.3865

Poschmann, M. (2018). *Atomistic Simulations of Screw Dislocations in Titanium* (Doctoral dissertation). University of California, Berkeley.

Poschmann, M., Asta, M., & Chrzan, D. C. (2017). Convergence of calculated dislocation core structures in hexagonal close packed titanium. *Modelling and Simulation in Materials Science and Engineering*, *26*(1), 014003. https://doi.org/10.1088/1361-651x/aa9ba9

Poschmann, M., Asta, M., & Chrzan, D. (2019). Effect of non-Schmid stresses on <a >-type screw dislocation core structure and mobility in titanium. *Computational Materials Science*, *161*(December 2018), 261–264. https://doi.org/10.1016/j.commatsci.2019.01.052

Poschmann, M., Winter, I. S., Asta, M., & Chrzan, D. C. (2022). Molecular dynamics studies of <*a*>-type screw dislocation core structure polymorphism in titanium. *Physical Review Materials*, *6*(1), 013603. https://doi.org/10.1103/PhysRevMaterials.6.013603

Rothchild, E., Poschmann, M., Asta, M., & Chrzan, D. (2022). Dislocation glide driven interstitial shuffling of oxygen interstitials in titanium. *Physical Review Materials*, *6*(9), 093601.

Sawyer, C. A., Morris, J. W., & Chrzan, D. C. (2013). Dislocation core radii near elastic stability limits. *Phys. Rev. B*, *87*, 134106. https://doi.org/10.1103/PhysRevB.87.134106

Schneider, T., & Stoll, E. (1978). Molecular-dynamics study of a three-dimensional one-component model for distortive phase transitions. *Physical Review B*, *17*(3), 1302–1322. https://doi.org/10.1103/PhysRevB.17.1302

Shimizu, F., Ogata, S., & Li, J. (2007). Theory of shear banding in metallic glasses and molecular dynamics calculations. *Materials Transactions*, *48*(11), 2923–2927. https://doi.org/10.2320/matertrans.MJ200769

Siems, R. (1968). Mechanical Interactions of Point Defects. *Physica Status Solidi (b)*, *30*(2), 645–658. https://doi.org/10.1002/pssb.19680300226

Stroh, A. N. (1958). Dislocations and cracks in anisotropic elasticity. *Philos. Mag.*, *3*(30), 625–646. https://doi.org/10.1080/14786435808565804

Stukowski, A. (2009). Visualization and analysis of atomistic simulation data with OVITO–the open visualization tool. *Modelling and Simulation in Materials Science and Engineering*, *18*(1), 015012. https://doi.org/10.1088/0965-0393/18/1/015012

Stukowski, A. (2010). Visualization and analysis of atomistic simulation data with OVITO-the Open Visualization Tool. *Modelling and Simulation in Materials Science and Engineering*, *18*(1). https://doi.org/10.1088/0965-0393/18/1/015012

Stukowski, A., Bulatov, V. V., & Arsenlis, A. (2012). Automated identification and indexing of dislocations in crystal interfaces. *Modelling and Simulation in Materials Science and Engineering*, *20*(8), 085007.

Suzuki, H. (1962). Segregation of solute atoms to stacking faults. *Journal of the Physical Society of Japan*, *17*(2), 322–325.

Takeuchi, S. (1999). Dislocation core effects on plasticity. *Radiation Effects and Defects in Solids*, *148*(1–4), 333–344. https://doi.org/10.1080/10420159908229099

Thompson, A. P., Aktulga, H. M., Berger, R., Bolintineanu, D. S., Brown, W. M., Crozier, P. S., in 't Veld, P. J., Kohlmeyer, A., Moore, S. G., Nguyen, T. D., Shan, R., Stevens, M. J., Tranchida, J., Trott, C., & Plimpton, S. J. (2022). Lammps - a flexible simulation tool for particle-based materials modeling at the atomic, meso, and continuum scales. *Computer Physics Communications*, *271*, 108171. https://doi.org/10.1016/j.cpc.2021.108171

Tsuru, T., Itakura, M., Yamaguchi, M., Watanabe, C., & Miura, H. (2022a). Dislocation core structure and motion in pure titanium and titanium alloys: A first-principles study. *Computational Materials Science*, *203*, 111081. https://doi.org/https://doi.org/10.1016/j.commatsci.2021.111081

Tsuru, T., Itakura, M., Yamaguchi, M., Watanabe, C., & Miura, H. (2022b). Dislocation core structure and motion in pure titanium and titanium alloys: A first-principles study. *Computational Materials Science*, *203*, 111081. https://doi.org/10.1016/j.commatsci.2021.111081

Varvenne, C., & Clouet, E. (2017). Elastic dipoles of point defects from atomistic simulations. *Phys. Rev. B*, *96*(22), 1–11. https://doi.org/10.1103/PhysRevB.96.224103

Varvenne, C., Luque, A., & Curtin, W. A. (2016). Theory of strengthening in fcc high entropy alloys. *Acta Materialia*, *118*, 164–176. https://doi.org/10.1016/j.actamat.2016.07.040

Vaughan, R., Blenkinsop, P., & Holl, H. (1980). The effect of oxygen content on the mechanical properties of an $\alpha + \beta$ titanium alloy ti-4al-2sn-4mo-0.5si (imi 550). *Titanium '80*.

Vítek, V., Perrin, R. C., & Bowen, D. K. (1970). The core structure of ½(111) screw dislocations in b.c.c. crystals. *The Philosophical Magazine: A Journal of Theoretical Experimental and Applied Physics*, *21*(173), 1049–1073. https://doi.org/10.1080/14786437008238490

Wallace, D. C. (1998). *Thermodynamics of crystals*. Courier Corporation.

Williams, J. C., & Luetjering, G. (1980). The Effect of Slip Length and Slip Character on the Properties of Titanium Alloys. *Titanium '80*, *1-6*, 671–681.

Winter, I. S., de Jong, M., Montoya, J., Rothchild, E., & Chrzan, D. C. (2019). Intrinsic ductility of random substitutional alloys from nonlinear elasticity theory. *Phys. Rev. Materials*, *3*, 113608. https://doi.org/10.1103/PhysRevMaterials.3.113608

Winter, I. S., Poschmann, M., Tsuru, T., & Chrzan, D. C. (2017). Dislocations near elastic instability in high-pressure body-centered-cubic magnesium. *Phys. Rev. B*, *95*, 064107. https://doi.org/10.1103/PhysRevB.95.064107

Wolf, K., Gudladt, H. J., Calderon, H. A., & Kostorz, G. (1994). Transition between planar and wavy slip in cyclically deformed short-range ordered alloys. *Acta Metallurgica Et Materialia*, *42*(11), 3759–3765. https://doi.org/10.1016/0956-7151(94)90441-3

Wu, H. H., & Trinkle, D. R. (2011). Direct diffusion through interpenetrating networks: Oxygen in titanium. *Physical Review Letters*, *107*(4), 045504. https://doi.org/10.1103/PhysRevLett.107.045504

Yu, Q., Qi, L., Tsuru, T., Traylor, R., Rugg, D., Morris, J. W., Asta, M., Chrzan, D. C., & Minor, A. M. (2015). Origin of dramatic oxygen solute strengthening effect in titanium. *Science*, *347*(6222), 635–639. https://doi.org/10.1126/science.1260485

Zhang, P., & Trinkle, D. R. (2016). A modified embedded atom method potential for interstitial oxygen in titanium. *Computational Materials Science*, *124*, 204–210. https://doi.org/10.1016/j.commatsci.2016.07.039